© 2026. Published by The Company of Biologists | Journal of Cell Science (2026) 139, jcs265302. doi:10.1242/jcs.265302

RESEARCH ARTICLE

SPECIAL ISSUE
IMAGING CELL ARCHITECTURE AND DYNAMICS

In situ visualization of autophagy reveals the presence of vesicles at the expanding phagophore rim

Claire Ortmann de Percin Northumberland[1,2], Mariya Licheva[3], Rahel Dabrowski[4], Rubén Gómez-Sánchez[5], Sabrina Berkamp[1,2], Philipp Schönnenbeck[1,2], Martin Graef[4,6], Claudine Kraft[3,7] and Carsten Sachse[1,2,*]

ABSTRACT

The autophagy core machinery mediates the enclosure of cytosolic cargo destined for degradation in the lysosome. The Atg9–Atg2–Atg18 complex coordinates phagophore expansion via directed lipid transfer until closure of the phagophore rim. Using an Atg2 variant (Atg2-PM4) as a model of decelerated autophagosome biogenesis, we visualized the morphological states prior to autophagosome closure by cryogenic correlative light and electron microscopy in *Saccharomyces cerevisiae*. Using *in situ* cryo-electron tomography, we find Atg2-PM4 cells have an enlarged rim morphology for an expanding phagophore in comparison with what is seen in the Atg2 wild-type condition. Analysis of segmented rim membrane features reveal surrounding and membrane-attached vesicles. The dimensions of the enlarged rims are consistent with fusion of cytosolic vesicles with the growing phagophore. High-resolution imaging in this study suggests that, apart from the initial nucleation phase, vesicle fusion can also contribute to phagophore expansion during later stages of autophagosome biogenesis.

KEY WORDS: Autophagy, Autophagosome biogenesis, Phagophore expansion, Atg2, Lipid transfer, Cryo-electron microscopy, Correlative light and electron microscopy, Membrane analysis

INTRODUCTION

Autophagy is a conserved homeostatic process that recycles molecular components of cellular material, such as damaged organelles and protein aggregates, by delivering them to the yeast and plant vacuole or the mammalian lysosome (Takeshige et al., 1992; Wen and Klionsky, 2016). The autophagic process can be triggered in response to cellular stresses, such as nutrient deprivation (Takeshige et al., 1992). There are three main types of autophagy: macroautophagy, microautophagy and chaperone-mediated autophagy (Xie and Klionsky, 2007). The morphological hallmark of macroautophagy (hereafter autophagy) is the *de novo* formation of a double-membrane compartment, the autophagosome, enclosing the autophagic cargo (Wen and Klionsky, 2016). To date, over 40 autophagy-related (Atg) proteins have been identified, initially in *Saccharomyces cerevisiae* (Tsukada and Ohsumi, 1993), with ∼18 belonging to the core autophagy machinery (Kawabata and Yoshimori, 2020; Nakatogawa, 2020). The autophagy machinery is organized in the following five evolutionarily conserved protein complexes – the Atg1 complex (Atg1, Atg13, Atg17, Atg29 and Atg31), the phosphatidylinositol-3 kinase (PI3K) complex (Atg6, Atg14, Vps34, Vps15 and Atg38), the Atg9–Atg2–Atg18 complex, the Atg12–Atg5 conjugation system (Atg12, Atg7, Atg10, Atg5 and Atg16), and the Atg8 conjugation system (Atg8, Atg7, Atg3 and Atg4) (Suzuki and Ohsumi, 2010; Noda, 2024; Nakatogawa, 2020). Autophagosome biogenesis temporally proceeds in five stages: phagophore initiation, nucleation, expansion, closure into an autophagosome and autophagosome fusion with the vacuole or lysosome (Wen and Klionsky, 2016).

After initiation in *S. cerevisiae*, the Atg1 complex forms the phagophore assembly site (PAS) at the surface of the vacuole to nucleate downstream assemblies of the PI3K and Atg9–Atg2–Atg18 complexes (Fujioka et al., 2020; Hollenstein et al., 2019). Atg9 is stored in Golgi-derived cytosolic vesicles prior to fusion at the PAS (Noda et al., 2000; Yamamoto et al., 2012). At the early stages of autophagy during nucleation, a subset of Atg9 vesicles localizes to the PAS and constitutes an initial membrane seed for formation of a phagophore (Sawa-Makarska et al., 2020; Olivas et al., 2023; Mari et al., 2010). In this context, Atg9-containing vesicles deliver autophagy factors as well as lipids to the nucleation site (Broadbent et al., 2023; Sawa-Makarska et al., 2020). COPII vesicles have also been implicated in the lipid supply to the phagophore (Graef et al., 2013; Shima et al., 2019). In mammalian autophagy, the ER–omegasome is the central platform for providing lipids for phagophore expansion (Axe et al., 2008; Hayashi-Nishino et al., 2009; Ylä-Anttila et al., 2009). Multiple membrane sources of the phagophore have been identified in mammalian cells, such as COPII vesicles, the ER-Golgi intermediate compartment (ERGIC) (Ge et al., 2014; 2013), mitochondria and mitochondria–ER contact sites (Hailey et al., 2010; Hamasaki et al., 2013), as well as recycling endosomes and the plasma membrane (Longatti et al., 2012; Ravikumar et al., 2010).

The growing phagophore (also called an isolation membrane) is derived from a cup-shaped membrane cisterna (Bieber et al., 2022; Shibutani and Yoshimori, 2014). During intermediate stages of

[1]Ernst-Ruska Centre for Microscopy and Spectroscopy with Electrons, ER-C-3/Structural Biology, Forschungszentrum Jülich, 52425 Jülich, Germany. [2]Department of Biology, Heinrich Heine University, Universitätsstr. 1, 40225 Düsseldorf, Germany. [3]Institute of Biochemistry and Molecular Biology, ZBMZ, Faculty of Medicine, University of Freiburg, Stefan-Meier-Str. 17, 79104 Freiburg, Germany. [4]Max Planck Research Group of Autophagy and Cellular Ageing, Max Planck Institute for Biology of Ageing, 50931 Cologne, Germany. [5]Department of Biomedical Sciences, University of Groningen, University Medical Center Groningen, A. Deusinglaan 1, 9713 AV Groningen, The Netherlands. [6]Department of Molecular Biology and Genetics, Cornell University, Ithaca, NY 14853, USA. [7]CIBSS-Centre for Integrative Biological Signalling Studies, University of Freiburg, Schänzlestr. 18, 79104 Freiburg, Germany.

*Author for correspondence (c.sachse@fz-juelich.de)

C.O.d.P.N., 0000-0002-2989-1463; M.L., 0000-0001-7722-7340; R.D., 0000-0002-3309-3851; R.G.-S., 0000-0002-8274-3259; S.B., 0000-0002-9639-9698; P.S., 0000-0002-6553-7517; M.G., 0000-0002-6820-1533; C.K., 0000-0002-3324-4701; C.S., 0000-0002-1168-5143

This is an Open Access article distributed under the terms of the Creative Commons Attribution License (https://creativecommons.org/licenses/by/4.0), which permits unrestricted use, distribution and reproduction in any medium provided that the original work is properly attributed.

Handling Editor: Giulia Zanetti
Received 29 August 2026; Accepted 7 September 2026

Journal of Cell Science (2026) 139, jcs265302. doi:10.1242/jcs.265302

autophagosome biogenesis, the core autophagy proteins Atg2 and Atg9 contribute to phagophore expansion – Atg2 by establishing membrane contact sites between the ER and ER exit sites (ERES) and the growing phagophore (together with the TRAPPIII complex) and mediating lipid transfer from a donor membrane (Gómez-Sánchez et al., 2025, 2018; Kotani et al., 2018; Maeda et al., 2019), and Atg9 by facilitating their distribution across both membrane leaflets (Chumpen Ramirez et al., 2023; Maeda et al., 2020; Matoba et al., 2020; Valverde et al., 2019). Atg9 is the only integral transmembrane protein among the core autophagy machinery components (Noda et al., 2000) and has been found to trimerize (Matoba et al., 2020). The scramblase activity of Atg9, which is essential for autophagy (Maeda et al., 2020; Matoba et al., 2020), is likely to contribute to maintaining previously reported lipid asymmetry in autophagic membranes, with higher phosphatidylinositol-3-phosphate (PI3P) levels in the luminal leaflets of both the outer and inner membranes than in the cytoplasmic leaflet of the outer membrane or the inner leaflet of the inner membrane (Cheng et al., 2014). Atg2 is an elongated rod-shaped β-helix protein found to supply lipids by bridging the phagophore to donor membranes (e.g. the ER) and providing a hydrophobic slide along its long axis that allows lipids to transfer from the N- to the C-terminal end of the rod (Chowdhury et al., 2018; Valverde et al., 2019). It has been shown that Atg2 has no lipid head-group transfer specificity (Osawa et al., 2019). A lipid transfer rate of 200 lipids per Atg2 molecule per second has been estimated *in vivo* using fluorescence microscopy (FM) to contribute to phagophore expansion (Dabrowski et al., 2023). It has also been found that Vps13, a homologue of Atg2 supports the lipid transfer to phagophores to render it non-rate limiting (Dabrowski et al., 2023).

Although the biochemical activities of both Atg2 and Atg9 in the context of autophagy have been characterized, how their respective functions are spatially and temporally coordinated to achieve a unidirectional lipid transfer to the growing phagophore remains under investigation. Two hypotheses have been put forward; the first one involving the *S. cerevisiae* long chain fatty acyl-CoA synthetase 1 (Faa1) and the second is based on two human scramblases TMEM41B and VMP1. Faa1 has been observed localizing to phagophores and generating acyl-CoA using ATP (Schütter et al., 2020). Subsequently, newly synthesized acyl-CoA is channelled to the phospholipid-synthesizing enzymes of the ER for *de novo* lipid synthesis. Newly synthesized lipids are subsequently transferred to the phagophore by Atg2. It has been proposed that *de novo* lipid synthesis increases the chemical potential, and thereby provides a driving force for the unidirectional lipid transfer from the ER into the phagophore (Schütter et al., 2020). The second hypothesis is based on the findings that deleting the two human scramblases TMEM41B and VMP1 resulted in depletion of autophagic flux (Morita et al., 2018) in addition to the described interaction with ATG2A at the ER (Ghanbarpour et al., 2021), providing a driver of unidirectional lipid transfer to the phagophore. In addition to the described mechanisms of lipid transfer, other cellular processes might contribute to phagophore growth.

Phagophore expansion is further accompanied by the conjugation of ubiquitin-like Atg8 to the phagophore membrane. The responsible machinery is composed of Atg5, Atg12 and Atg16 (Romanov et al., 2012) and acts like an E3 ligase complex to transfer Atg8 from Atg3 to membrane-resident phosphatidylethanolamine (Hanada et al., 2007). Phagophore expansion through lipids and Atg8 conjugation proceeds until the phagophore rims are ready to be fused to form a closed autophagosome. Deletion of *S. cerevisiae* Snf7 as well as human *CHMP2B* and *VPS4* leads to an accumulation of unsealed phagophores and consistently impaired autophagosome completion (Takahashi et al., 2018; Zhou et al., 2019). Snf7 and CHMP2B belong to the family of ESCRT-III proteins enabling membrane fusion and/or fission, and in this case, they mediate the closure of phagophores into double-membrane autophagosomes. Impaired ESCRT-mediated trafficking has been characterized in yeast by following, for example, Vps8, a peripheral membrane protein associating with endosomal membranes, leading to an accumulation in so-called class E compartments (Russell et al., 2012). Ypt7 is the yeast Rab7 homologue serving as the master fusion GTPase that is responsible for endosome as well as autophagosome fusion with the vacuole (Kim et al., 2001; Schimmöller and Riezman, 1993).

Single-particle cryo-electron microscopy (cryo-EM) has generated a wealth of structural insights on the large multi-protein complexes of autophagy based on biochemical isolations (Berkamp et al., 2025; Ciuffa et al., 2015; Jakobi et al., 2020; Maeda et al., 2020; Matoba et al., 2020; Wang et al., 2025). Owing to a number of technological advancements, the near-native cellular visualization of the autophagy process in frozen-hydrated cells has also recently become possible and revealed the details of membrane biogenesis stages in yeast and human cells (Berkamp et al., 2025; Bieber et al., 2022; Li et al., 2023). Correlative light and electron microscopy (CLEM) of autophagy-specific protein markers, such as Atg8 and p62 (also known as SQSTM1) enabled the targeted visualization of the dynamic autophagy process after plunge-freezing of cells (Berkamp et al., 2023; Capitanio et al., 2023). Despite the progress in detailed mapping of autophagy biogenesis stages, the detection of transient molecular events remains challenging. Currently, detection of autophagy events is possible, but the preparation of 100–200 nm thin lamella slices of cells by a focused ion beam milling scanning electron microscope (FIB-SEM) removes most of the cellular volume including the events of interest. Therefore, typically various enrichment strategies, such as blocking of autophagosome fusion or autophagy progression, have to be employed to visualize autophagy events at this level of detail (Berkamp et al., 2025; Bieber et al., 2022).

The interaction between Atg2 and Atg9 has also been shown to be essential for autophagic turnover (Gómez-Sánchez et al., 2018). When disrupting the Atg2–Atg9 interaction using point mutations at the C-terminal region of Atg2 (named Atg2-PM4), both Atg9 and Atg2 still concentrate at the phagophore membrane, but in different locations. Although Atg9 and Atg2 both localize to the phagophore rims, mutant Atg2-PM4 mislocalizes, showing distribution along the phagophore membrane distal from the rims (Gómez-Sánchez et al., 2018). It has been suggested that the association of ER and phagophore is altered as a result (Gómez-Sánchez et al., 2018). Here, we characterized the Atg2-PM4 mutant by live-cell fluorescence microscopy revealing it causes delayed phagophore formation. Moreover, we visualized the native accumulated phagophores in the Atg2-PM4 mutant *S. cerevisiae* cells using *in situ* cryo-ET coupled with cryo-CLEM and observed significantly enlarged phagophore rims upon disruption of the Atg2–Atg9 interaction. The tomograms provide evidence of vesicular attachment to the phagophore and suggest that vesicle fusion can contribute to lipid growth at intermediate stages of autophagosome biogenesis during phagophore expansion.

RESULTS

Phagophore formation is decelerated in Atg2-PM4-expressing cells

To better understand phagophore expansion and morphology, we focused on the Atg9–Atg2 interaction and turned to the previously

Journal of Cell Science (2026) 139, jcs265302. doi:10.1242/jcs.265302

characterized Atg2-PM4 mutant (Gómez-Sánchez et al., 2018), which carries five mutations in the C-terminal region (QKFST to AAAAA; 1264–1268) (highlighted in AlphaFold 3 model; Fig. S1), disrupting the interaction of Atg2 with Atg9 at the phagophore. For this, we used live-cell fluorescence imaging to characterize autophagosome biogenesis and imaged phagophores in cells expressing mCherry–Atg8, as described previously (Dabrowski et al., 2023), together with Atg2-WT–3xGFP (wild-type Atg2) and Atg2-PM4–3xGFP, respectively [Fig. 1A; expressing wild-type (WT)]. Interestingly, in Atg2-PM4 cells, we were unable to detect Atg2-PM4 puncta as opposed to what was seen in the Atg2-WT control, which is consistent with previous studies suggesting that the Atg2-PM4 mutant distributes across the phagophore membrane rather than accumulating at the phagophore rims (Gómez-Sánchez et al., 2018). When counting the number of Atg8 puncta per cell, we observed a slight decrease for Atg2-PM4 cells, although the overall variation was very similar to that of Atg2-WT cells (Fig. 1B, left). More importantly, on average we found less than one closed phagophore per five cells (i.e. 0.2 phagophores per cell) in Atg2-PM4 cells compared with 0.7 closed phagophores per cell in Atg2-WT (Fig. 1B, right). These results indicate that the autophagosome formation rate might have been affected in the Atg2-PM4 mutant. To investigate this hypothesis, we performed timelapse fluorescence microscopy and followed Atg8 puncta from nucleation until autophagosome fusion with the vacuole, for a maximum of 30 min (as previously described in Dabrowski et al., 2023). This way, we visualized small initial membrane seeds as Atg8 puncta and expanding phagophores or autophagosomes as Atg8-marked patches or ring-like structures over time and observed an increase in the total lifetime of Atg8 positive structures in Atg2-PM4 mutant cells when compared with Atg2-WT cells, on average lasting 22 versus 10 min in the Atg2-WT (Fig. 1C). Taken together, the fluorescence analyses of the Atg2-PM4 mutant revealed that autophagosome biogenesis was decelerated resulting in lower numbers of autophagosomes than in the Atg2-WT.

Establishing the *snf7Δ* yeast strain to cause phagophore accumulation

In order to enrich phagophore expansion events for downstream cryo-EM studies, we turned to a *snf7* deletion (*snf7Δ*) strain that has been shown to accumulate open (i.e. unsealed) phagophores at the vacuole (Zhou et al., 2019). At the same time, it had been characterized by vesicle trafficking defects and large endosomal structures named class E compartments (Raymond et al., 1992). We wanted to verify that these altered membrane dynamics did not affect phagophore biogenesis. To exclude this possibility, we therefore followed Vps8 foci to visualize class E compartments, as Atg8 has been previously shown to concentrate in these clusters upon ESCRT-III dysfunction (Russell et al., 2012). We turned to live-cell imaging to monitor Vps8–mScarlet foci alongside GFP–Atg8 in *atg2Δ*, Atg2-WT and Atg2-PM4 cells with the acidic vacuoles stained by CMAC in *snf7Δ* background cells, respectively (Fig. 2A). When we estimated the fraction of Vps8 spatially close to Atg8, we observed that ∼25% of Atg8-positive structures associated with class E compartments between the different strains (showing 20, 32 and 23% association for *atg2Δ*, Atg2-WT, and Atg2-PM4 cells, respectively) (Fig. 2B). As expected, we observed the presence of larger GFP–Atg8 foci in both Atg2-WT and Atg2-PM4 cells, when compared with *atg2Δ* cells, in line with previous studies (Gómez-Sánchez et al., 2018; Chumpen Ramirez et al., 2023). These differences in fluorescence intensity and clustering between Atg2-WT and Atg2-PM4 cells can be explained by the defective recruitment of Atg18 to the nascent phagophore in Atg2-PM4 cells (Gómez-Sánchez et al., 2018).

Although Atg2–Atg9 binding is disrupted in the Atg2-PM4 mutant, previous studies have shown that Atg9 is able to localize at the phagophore rims (Gómez-Sánchez et al., 2018). In order to exclude the possibility of an altered Atg9 distribution in *snf7Δ* cells, we took advantage of an established live-cell microscopy assay based on the overexpression of Ape1 protein leading to the generation of a giant Ape1 oligomer and allowing the visualization of phagophores (Suzuki et al., 2013). Notably, Atg9 was found to be localized at the rims of the growing phagophore in both Atg2-WT and Atg2-PM4 *snf7Δ* cells (Fig. 2C), whereas no phagophore was formed in *atg2Δ snf7Δ* cells, in agreement with previous studies (Gómez-Sánchez et al., 2018). These data indicate that Atg9 distribution at the phagophore membrane is not affected by the absence of Snf7. Taken together, these live-cell imaging data indicate that the growing phagophores in the Atg2-PM4 mutant *snf7Δ* strain do not show increased association with class E compartments or Atg9 mislocalization, supporting the conclusion that the *snf7Δ* strain presents a suitable experimental model to further visualize phagophore biogenesis.

Visualization of phagophores in *snf7* deletion cells by *in situ* cryo-ET

In order to study expanding phagophores of *S. cerevisiae* at higher resolution, we employed *in situ* cryo-ET and continued to work with the *snf7Δ* strain (Fig. 3A). To identify the region of interest for tomographic data acquisition, we were guided by Atg9–3xmTagBFP2-positive puncta using cryo-CLEM. When we detected a BFP signal to validate the presence of Atg9, we generated cellular lamellae with a focused ion beam milling scanning electron microscope (FIB-SEM) operated at cryogenic temperatures (Fig. 3B) and correlated in-chamber fluorescence images after milling (Fig. 3C) with transmission electron microscopy (TEM) overview images (Fig. 3D,E). In this way, we acquired a total of 13 tomograms of ∼150–200 nm thickness and visualized six sections through phagophores in cells with WT autophagy machinery including WT Atg2 (Atg2-WT) (Fig. 3F, Table 1). We observed characteristic phagophores of 300–400 nm in diameter with their closely apposed bilayers in proximity to the ER and lipid droplets (Fig. 3G,H). Occasionally, extended densities were identified as membrane connections ∼20 to 24 nm in length (Table 2) bridging the phagophore membrane to putative donor membranes [the ER (Fig. 3G*, red arrowheads) and lipid droplet surfaces (Fig. 3H*, red arrowheads)]. These densities match the length of the mammalian Atg2 and yeast Vps13p molecules (Valverde et al., 2019; De et al., 2017). The phagophores imaged in the Atg2-WT *snf7Δ* strain (Fig. 3G–I) are consistent with previously observed phagophore ultrastructures in *ypt7Δ* cells with the characteristic cup-shaped membrane, as well as protein-mediated membrane contact sites with the phagophore (Bieber et al., 2022). As phagophores accumulate in the cytosol of *snf7Δ* cells and are prevented from fusing with the vacuole, we successfully observed multiple stages of phagophore expansion in Atg2-WT conditions of this otherwise highly transient process.

Phagophore morphology is altered in the Atg2-PM4 mutant

Using the above-described cryo-CLEM workflow with Atg2-PM4 *snf7Δ cells*, we observed a striking Atg2-PM4 phenotype with respect to phagophore morphology: 16 out of 25 phagophore rims revealed an enlarged intermembrane spacing of 50 up to 200 nm when analysed in *z*-section (Fig. 4A–F, blue arrowheads). The

Journal of Cell Science (2026) 139, jcs265302. doi:10.1242/jcs.265302

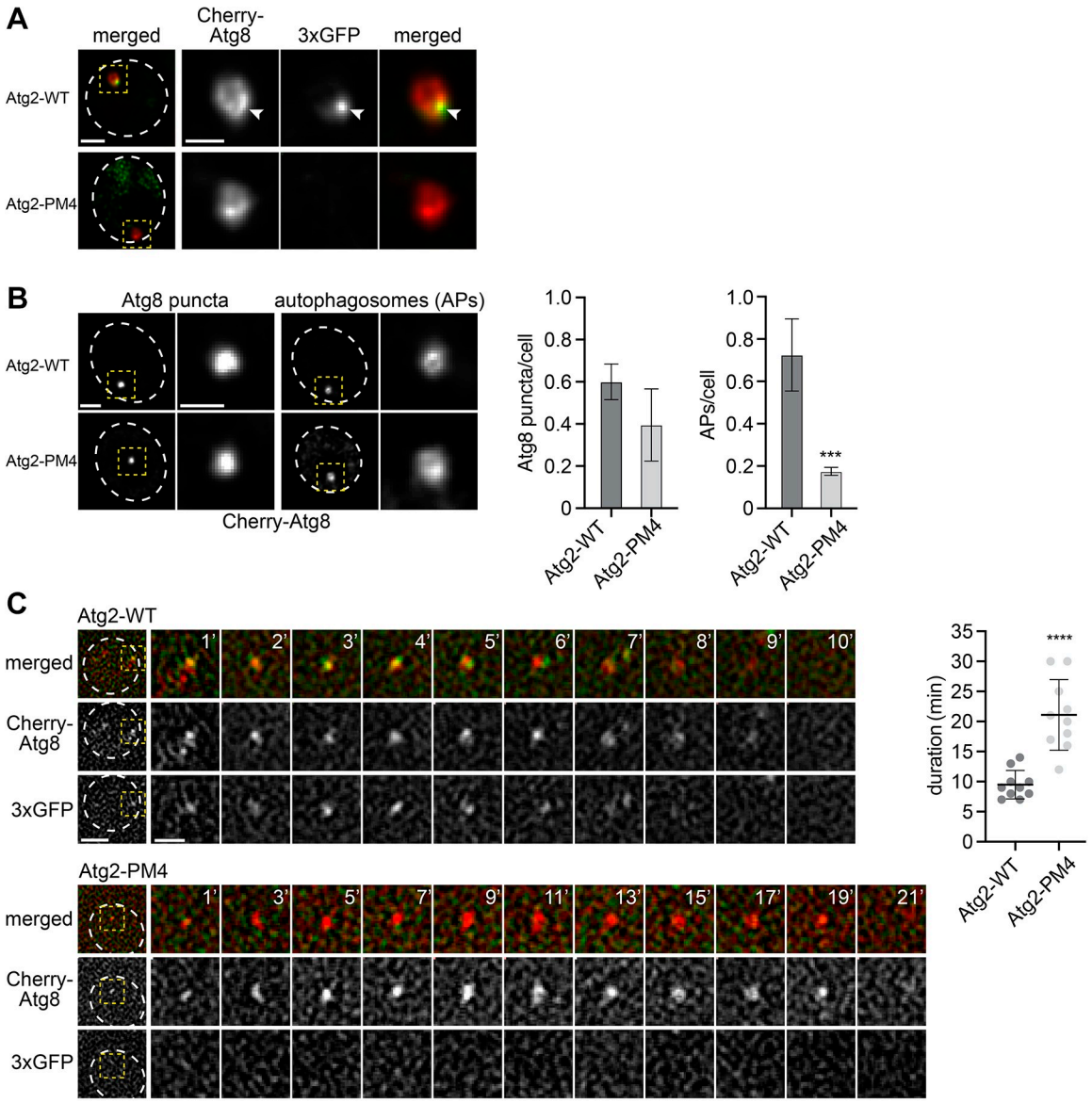


Fig. 1. Fluorescence light microscopy live-cell imaging of autophagosome biogenesis in Atg2-PM4 cells and imaging of Atg8- and Vps8-positive structures. (A–C) Representative live-cell fluorescence microscopy images of cells expressing Atg2-WT–3xGFP or the Atg2-PM4–3xGFP mutant together with mCherry-ATG8 (W303 strain). Images were acquired after 1 h of nitrogen starvation. Dashed white lines and yellow rectangles indicate cell boundaries and magnified areas, respectively. (A) White arrowheads indicate position of Atg2–3xGFP punctum localized to an autophagosome. (B) Representative images of Atg8 puncta and autophagosomes are shown for both strains in the left panel. Quantifications of the relative number of Atg8 puncta and autophagosomal/phagophore structures (APs) per cell of indicated strains are shown in the right panel (n=4; 200 structures analysed in total/strain). (C) Representative timelines of autophagosome biogenesis events of indicated strains. Quantification of live-cell timelapse fluorescence imaging. Duration describes the time from nucleation (timepoint 1′, where ′ represents time in minutes) until fusion with the vacuole (last timepoint shown), as described previously (Dabrowski et al., 2023) (n=2; 10 events/strain). All error bars show mean±s.d. ***P<0.0002; ****P>0.0001 (two-tailed unpaired t-tests). Scale bars: 2 µm (whole cell); 1 µm (magnifications).

remaining nine rims resembled the Atg2-WT phenotype with a small widening of close-to evenly distanced juxtaposed bilayers spaced ∼10 to 20 nm apart (Fig. 4G–I, orange arrowheads) as previously characterized (Bieber et al., 2022). Interestingly, when seen in cross-section, one specific phagophore had one enlarged rim region and the corresponding rim region on the other side of the same phagophore appears to be Atg2-WT-like (see Fig. 4B, blue and orange arrowheads). Others exhibited either uniformly Atg2-WT-like rims or two enlarged rims. When inspecting membrane contact sites, as in the Atg2-WT, we also detected connecting protein densities spanning from the phagophore to putative donor membranes (Fig. 4J,H*). Notably, two of these tethering densities were 29 nm in length (Table 2), which is 9 nm longer than mammalian ATG2 and Vps13 but corresponds to the predicted length of the yeast protein Csf1, another bridge-like lipid transfer protein (Toulmay et al., 2022; Valverde et al., 2019; De et al., 2017). Another extended density of 23 nm length tethering the phagophore to the lipid droplet surface is closer to the observed length of ATG2 and Vps13 (Valverde et al., 2019; De et al., 2017). Furthermore, we also observed a direct membrane contact site between the phagophore and lipid droplet not obviously bridged by protein density. The outermost bilayer of the phagophore was found

Journal of Cell Science (2026) 139, jcs265302. doi:10.1242/jcs.265302

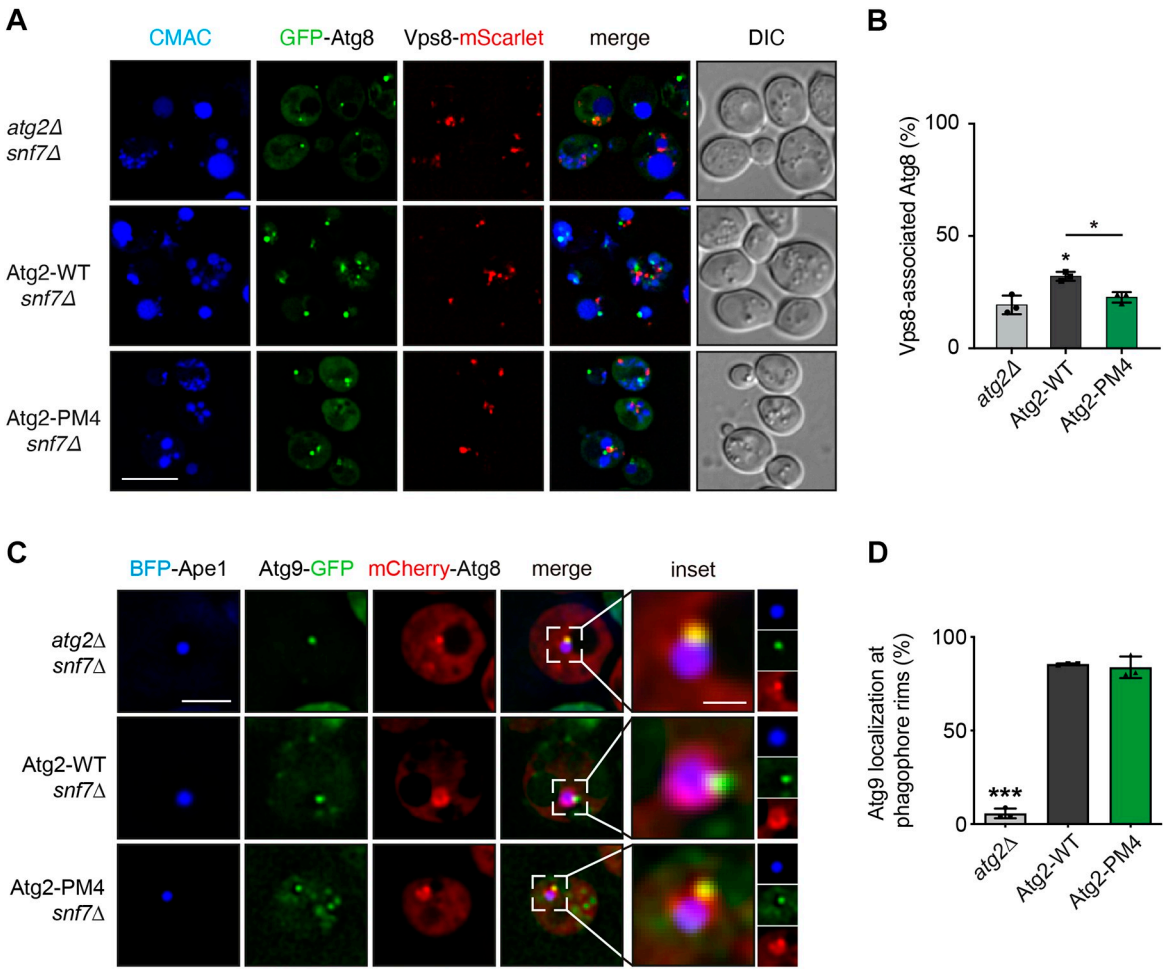


Fig. 2. Imaging of Atg8 and Vps8-positive structures and Atg9 distribution at the phagophore. (A) The *snf7Δ atg2Δ* strain (BY) expressing GFP–Atg8 and Vps8–mScarlet (RGY1381,) was transformed with an empty vector (pRS416; *atg2Δ*) or plasmids expressing Atg2-WT or Atg2-PM4 mutant. CMAC staining highlights acidic vacuoles (blue). Transformed cells were cultured in SD-URA to early log phase and transferred into SD-N starvation medium for 2 h to induce autophagy before being analysed by live-cell imaging. DIC, differential interference contrast. (B) The percentage of GFP–Atg8-labelled PAS associated with Vps8–mScarlet foci in the experiment shown in A (three independent experiments; mean±s.d.). **P*<0.05 (the asterisk above the horizontal bar highlights significant differences between *atg2Δ* and Atg2 cells; the asterisk above the Atg2-WT result indicates significant difference between Atg2 and Atg2-PM4 cells; two-tailed unpaired *t*-test with Welch's correction). (C) The *snf7*Δ *atg2*Δ strain carrying endogenous Atg9–GFP and mCherry–Atg8 (RGY1428) with or without an integrative plasmid expressing Atg2-WT (RGY1429) or Atg2-PM4 (RGY1427) were transformed with the pDP105 plasmid to generate giant BFP–Ape1 oligomers. Cells were grown to induce the formation of giant Ape1 oligomers and then analysed by live-cell imaging as described in the Materials and Methods. (D) Quantification of Atg9 distribution on the mCherry–Atg8-positive phagophores in the experiment shown in C (three independent experiments; mean±s.d.). ****P*<0.05 (with the strain carrying Atg2-WT; two-tailed unpaired *t*-test with Welch's correction). Scale bars: 4 µm (A), 2 µm (C, main images), 0.5 µm (C, magnified view).

touching the phospholipid monolayer of the lipid droplet surface giving up the otherwise close-to-ideal spherical shape and leaving an increased intermembrane distance of the phagophore at the region of contact (Fig. 4I*). Together, this Atg2-PM4 ultrastructural analysis reveals a remarkable Atg2-PM4 phenotype of enlarged phagophore rims and that these cells also contain some typical and some thus far unobserved protein-mediated membrane contact sites between phagophores and putative donor membranes.

Analysis of enlarged rims and associated membrane structures

To assess the morphological changes of the Atg2-PM4 phagophores in more detail, we specifically analysed the phagophores from the cryo-tomograms using segmentation and grouped the Atg2-PM4 phagophore rim sections into 'enlarged' and 'thin' classes. As we evaluate representative 2D sections through the 3D tomogram, we refer to phagophore ends as tips rather than the rim, which is part of the specific 3D cup structure, because the tip represents the herein visualized cross-section of a phagophore. Subsequently, we computationally separated the tip region next to the backbone region of the phagophore making up the central portion of the phagophore (Fig. 5A). Comparison of membrane segmentations of the phagophore rims from representative tomographic slices of the Atg2-PM4 enlarged class showed marked differences to the Atg2-WT and the Atg2-PM4 thin classes (Fig. 5B). Whereas the intermembrane distances of the backbone region of Atg2-WT, Atg2-PM4 enlarged and thin phagophore classes shared similar widths of 135±25 Å, 119±29 Å and 135±29 Å (1 Å=0.1 nm; mean±s.d.), respectively (Fig. 5C), the intermembrane distance at the tip (tip width) of the Atg2-PM4 enlarged class is 284±91 Å as opposed to 127±10 Å and 131±26 Å of Atg2-WT and Atg2-PM4 thin, respectively (Fig. 5D). When estimating the curvatures of the

Journal of Cell Science (2026) 139, jcs265302. doi:10.1242/jcs.265302

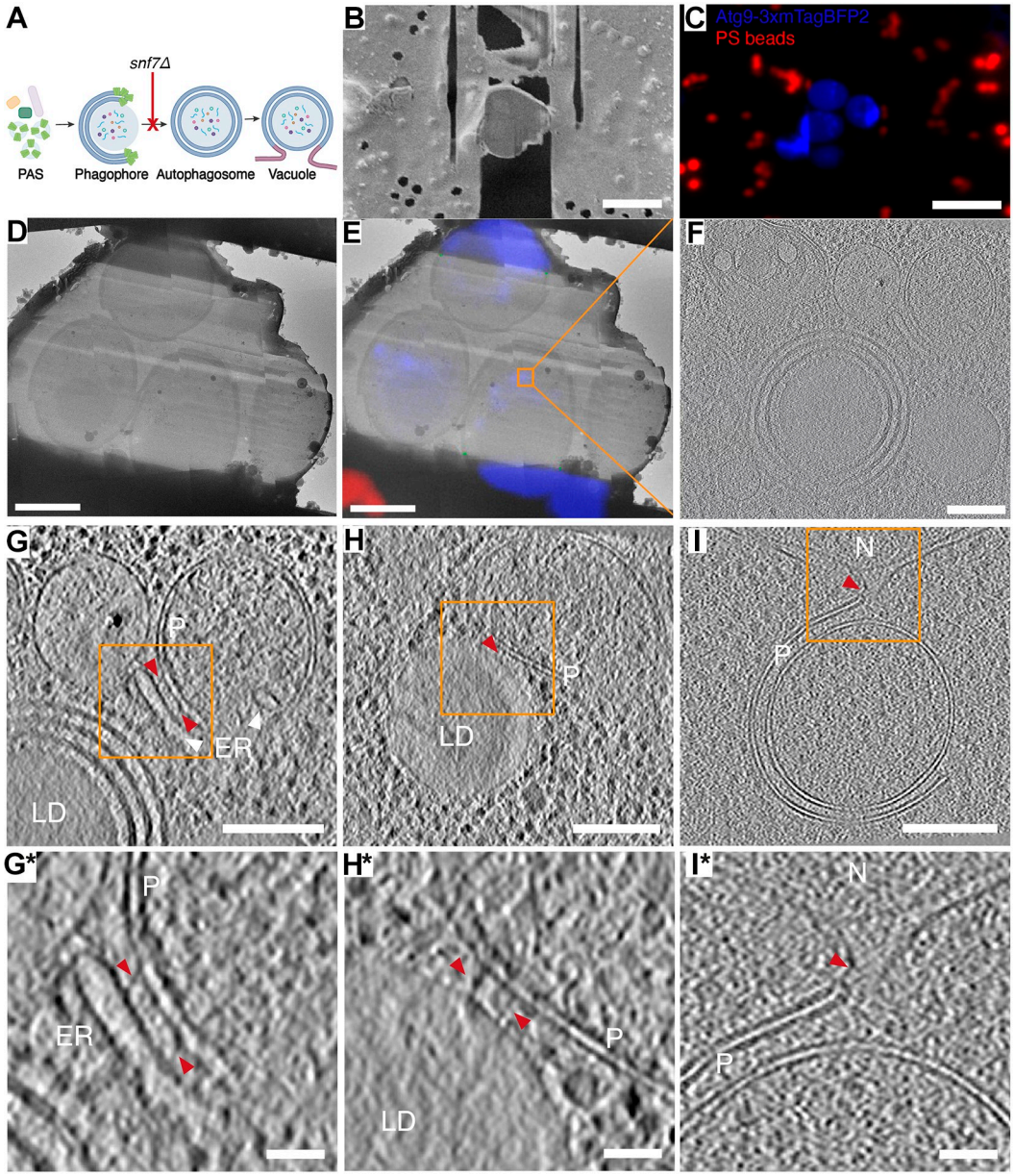


Fig. 3. Visualization of yeast phagophores by correlative light and electron microscopy. (A) Schematic representation of autophagosome biogenesis including phagophore closure mediated by Snf7 that was deleted for the analysis. (B) SEM image of yeast cellular lamella used to characterize WT phagophore elongation in *snf7Δ* cells. (C) Same lamella as in B imaged in a fluorescence microscope under cryogenic conditions. Signal shown in blue represents Atg9–3xmTagBFP2, and signal shown in red originates from polystyrene (PS) fiducial beads. (D) TEM overview of the same lamella as shown in B and C. (E) TEM overview of lamella (D) correlated with the fluorescence image of same lamella (C). Region on which tilt series was acquired is indicated by orange box. (F) Tomographic slice of multiple tomograms showing phagophore, acquired from the region indicated in E. (G–I) Tomographic slices of phagophores from *snf7Δ* yeast cells, denoised with IsoNet (Liu et al., 2022). (G*–I*) Enlarged views of regions from panels G–I marked with orange boxes. Red arrowheads in panels G–I* show densities spanning from a donor membrane to the phagophore membrane; measured lengths are listed in Table 2. Phagophores are indicated with P, lipid droplets with LD, endoplasmic reticulum with ER, vacuole with V, nucleus with N. For B–E, images representative of more than 20 repeats. For panels F–I, images representative of 6 collected tomograms containing phagophore rims. Scale bars: 10 µm (B,C), 3 µm (D,E), 200 nm (F–I), 100 nm (G*–I*).

inner and outer phagophore bilayers omitting the utmost tip region region (grey segment with arrowhead in Fig. 5B), the average of the maximum absolute curvatures of the Atg2-PM4 enlarged tips is significantly higher than the those for the Atg2-WT and Atg2-PM4 thin class at 1.6×10^{-3} Å^{-1} versus 0.9×10^{-3} Å^{-1} and 0.9×10^{-3} Å^{-1}, respectively (Fig. 5E). In agreement, the Atg2-PM4 enlarged tips have a lower percentage of pixels with lower absolute curvatures, and more pixels with higher absolute curvatures than the Atg2-WT and Atg2-PM4 thin phagophore tips (Fig. 5F). In order to understand whether the changes observed at the phagophore rim are related to the progression of phagophore growth, the rim opening angle of every tip section was estimated and related to the average tip width. The rim opening angle has been proposed as a measure of phagophore growth (Bieber et al., 2022) whereby this angle ranges from close to 0° when the phagophore is barely cup-shaped, to 180° when the tips are nearly facing each other head-on before fusing

Journal of Cell Science (2026) 139, jcs265302. doi:10.1242/jcs.265302

Table 1. Summary of cryo-electron tomography data collection

	Total tomograms collected	Tomograms containing phagophore rims	Acceleration voltage (keV)	Cell culture batch
Total	30	17		
Atg2-WT	13	2	200	Batch 1
		4	300	Batch 2
Atg2-PM4	17	4	200	Batch 1
		7	200	Batch 2

with each other (Fig. 5G). When plotting the rim opening angle against the mean tip width, we detected a weak linear positive trend for Atg2-WT and the Atg2-PM4-thin tips between 60 and 160° in Atg9–3xBFP cells (Fig. 5H), which appears to differ from previous observations proposing a negative trend in WT cells with GFP-Atg8 background (Bieber et al., 2022). The analysis of the Atg2-PM4-enlarged tip class, however, clearly revealed wider rim opening angles between 0 and 140° and widely scattered tip width measurements between 150 and 450 Å, supporting no clear trend. Taken together, the detailed distance, angle and shape analysis based on membrane segmentation confirmed that the observed morphological changes are significantly different in the Atg2-PM4 enlarged class and restricted to the phagophore rim, whereas the phagophore backbone appears similar to the Atg2-WT.

When further inspecting our Atg2-PM4 tomographic data, we noticed the occurrence of vesicles in the proximity of up to 200 nm from phagophore rims (Fig. 6A–E; Fig. S2). The phagophores near to these vesicles were found in different stages of expansion and varied in length and rim opening angles. Atg2-WT tomograms did not contain such vesicles. Atg2-PM4 vesicles varied in circularity and in size, with diameters ranging from 37 to 187 nm (Table 3). Subsequently, in one particular tomogram, we also observed one phagophore with rim sections as wide as typical vesicle diameters, of between 150 and 190 nm (Fig. 6F,G). After membrane segmentation of the tomographic reconstruction displayed as a 3D isosurface rendering (Fig. 6H), we observed an ∼180 nm thick slab through the membrane phagophore, whereas we discerned two ∼200-nm-wide distinct membrane entities consistent with two fusing vesicles attached to enlarged phagophore rims on opposite ends of the phagophore connected through a ∼100-nm-wide membrane stalk. In the 3D rendering of the segmentation, the vesicles did not appear completely closed, which can be attributed to the missing wedge, a known sampling problem in electron tomography (Förster and Briegel, 2024). Taken together, in one of the tomograms, we captured additional density on the phagophore rims consistent in dimension with cellular vesicles attached to an expanding phagophore.

As COPII coat proteins such as Sec13 and Sec31 have been observed by fluorescence microscopy to localize at the phagophore rims (Graef et al., 2013; Suzuki et al., 2013) and COPII vesicles have been identified as an important lipid source for autophagosome biogenesis in yeast (Shima et al., 2019), we therefore checked for the presence of characteristic protein lattice coats on the vesicles proximal to the phagophore rims (Fig. S3). In these cases, we could not identify typical features of clathrin, COPII or COPI lattice coatings, such as distinct triskelion of clathrin or the triangular Sec13–Sec31 COPII structure (Bykov et al., 2017; Cheng et al., 2007; Zanetti et al., 2013). Moreover, typical COP vesicles surrounding the Golgi network have been found to be ∼50 nm (Bykov et al., 2017; Donohoe et al., 2013) whereas many of the observed vesicles here were larger than 100 nm. Our data on these vesicular features do not allow an assignment and leave the cellular origin of them open. The observed vesicles close to the phagophore rims are unlikely to be a result of aberrant endosomal processing in the *snf7Δ* strain as they were not detected in Atg2-WT *snf7Δ* cells (see Fig. 2A,B), but rather belong to membranous structures of different subcellular identity. Taken together, the presence of medium-sized 40–200 nm vesicles close to the phagophore rims and in some cases enlarged rims of the same size suggest vesicle fusion to the rims of the phagophore in Atg2-PM4 cells.

Table 2. Length of densities tethering phagophore and putative donor membranes in both Atg2-WT and Atg2-PM4 cells

Phenotype	Measured length (nm)	Figure
Atg2-WT	20	Fig. 3G* (top)
	21	Fig. 3G* (bottom)
	24	Fig. 3H* (top)
	23	Fig. 3H* (bottom)
Atg2-PM4	29	Fig. 4H* (top)
	29	Fig. 4H* (bottom)
	23	Fig. 4J

DISCUSSION

Using *in situ* cryo-ET guided by cryo-CLEM, we imaged and analysed the natively preserved morphology of expanding phagophores of *snf7Δ S. cerevisiae* strains. We observed multiple phagophore–membrane contact sites including direct lipid droplet contact and linkages mediated by bridge-like proteins. Using a previously characterized Atg2-PM4-mutant unable to interact with Atg9 (Gómez-Sánchez et al., 2018), we found an altered phagophore morphology. The Atg2-PM4 mutant revealed an approximately twofold enlarged phagophore rim width, while it also showed a significantly decelerated autophagosome biogenesis in live-cell imaging. As we observed the presence of 40 to 200 nm large vesicles in close proximity to phagophore rims and captured vesicles attached to a phagophore, we reason that the enlarged rims in our tomographic data represent an intermediate structure resulting from vesicular fusion to the phagophore rims in a lipid-transport impaired mutant.

The disruption of the Atg2–Atg9 interaction caused by the alanine substitutions in positions 1264–1268 in the Atg2-PM4 mutant clearly affected the observed phagophore morphology leading to enlarged phagophore rims. Owing to the disrupted interaction with Atg9, Atg2 was found mislocalized across the entire phagophore in contrast to Atg9 and Atg18 that remained localized at the phagophore rims (Gómez-Sánchez et al., 2018). As a consequence of disrupted Atg9 interaction by another mutant, a reduction of the human Atg2 *in vitro* lipid transfer activity has been reported (Van Vliet et al., 2022). Moreover, *in vitro* Atg2 lipid transfer has been shown to increase in the presence of Atg18 and PI3P (Osawa et al., 2019). Therefore, the disruption of described Atg2 interactors is likely to have an overall attenuating effect on Atg2-mediated lipid supply to the phagophore. Given the close spatial coupling and proposed lipid channelling of Atg2 with Faa1 and Atg9 (Schütter et al., 2020; Van Vliet et al., 2022; Wang et al., 2025), the effective lipid transport and subsequent lipid equilibration across the leaflets is likely to be altered in the Atg2-PM4 mutant. The disruption of Atg2–Atg9 interaction might lead to a defective redistribution of incoming lipids between the two bilayers of the phagophore and thus give rise to the observed Atg2-PM4 phenotype rim morphologies. Under WT conditions, owing to

Journal of Cell Science (2026) 139, jcs265302. doi:10.1242/jcs.265302

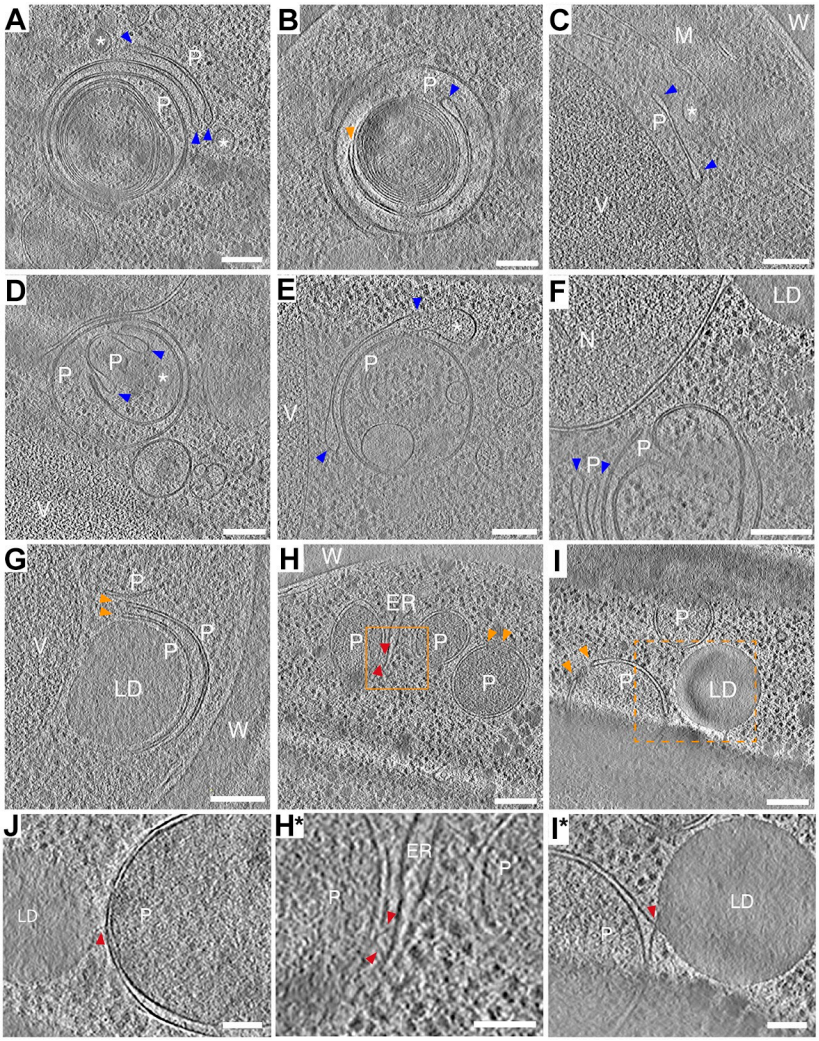


Fig. 4. Tomogram slices of phagophore ultrastructures in Atg2-PM4 cells. (A–I*) Tomographic slices of multiple tomograms from Atg2-PM4 mutant yeast cells, denoised with IsoNet (Liu et al., 2022). Blue arrowheads indicate the increased intermembrane space of phagophores located at the enlarged rims. Orange arrowheads indicate rim ends that have the same intermembrane distance as the WT phagophores. Red arrows indicate elongated densities spanning from the phagophore membrane to the ER or lipid droplets, measured lengths of such densities are listed in Table 2. (H*) Enlarged view of tomogram slice shown in H (orange box). (I*) Enlarged view from a different tomographic *z*-slice from the tomogram shown in I (dashed orange box). Phagophores are indicated with P, lipid droplets with LD, endoplasmic reticulum with ER, vacuole with V, nucleus with N, and the cell wall with W. Asterisks indicate vesicles of unknown origin. Images representative of 13 tomograms containing phagophore rims. Scale bars: 200 nm.

the close spatial coupling, Atg2 provides lipid substrates unidirectionally for the Atg9 scramblase (Fig. 7A). In the Atg2-PM4 mutant, the lack of unidirectional lipid substrate provision for Atg9 might affect the lipid turnover (Fig. 7B, left), possibly leading to changes in the rim shape considering principal membrane geometry arguments (Frolov et al., 2011). It should be added that the exact effect of the Atg2–Atg9 interaction on the scramblase activity of Atg9 is still under investigation. A recent preprint by Cabezudo and colleagues hypothesized, based on AlphaFold3 predictions and molecular dynamics simulations, that human ATG2A does not directly handover lipids to ATG9A and that the mutations in Atg2-PM4 are therefore unlikely to lie at the interface (Cabezudo et al., 2025 preprint). This hypothesis, however, contrasts with what is shown in cryo-EM structures of mammalian Atg2A, where ATG9A is positioned in a way suggesting more direct lipid transfer between ATG2A and ATG9A (van Vliet et al., 2022; Wang et al., 2025).

Another recent study has examined the role of various autophagy factors on the rim morphology of the phagophore in *S. cerevisiae* (Shatz et al., 2024). Partial depletion of Atg2 or Atg18, but not Atg9, was shown to lead to an opening of the phagophore rim. Moreover, cells with investigated Atg24 mis-localization mutants show changes in the overall phagophore morphology as visualized by live-cell fluorescence microscopy (Shatz et al., 2024). In that study, the rim morphology was also visualized by high-pressure freezing freeze-substitution CLEM. However, the features of the here-reported enlarged natively preserved cryo-ET rim sections of the Atg2-PM4 mutant were not observed but the detailed comparison of membrane fine structure is difficult due to differences in magnification, interpretable resolution and preparation conditions. The here-examined phagophores of the Atg2-PM4 mutant displayed significant changes in the fine structural morphology with enlarged rim opening angles and a disrupted correlation between mean rim width and rim opening angle relative to WT-like rims. In line with a series of prior studies, our investigation further supports the requirement of precise temporal and spatial localization of Atg9–Atg2–Atg18 complexes at the phagophore for autophagosome biogenesis. The observation of a putative vesicle–phagophore fusion event to an expanding phagophore in cells with decelerated autophagosome biogenesis when compared with WT cells might arise from two possible scenarios. First, in Atg2-WT cells the fusion event might be too transient to be captured by our cryo-CLEM approach while it is slower and becomes detectable in the Atg2-PM4 mutant. Second, the Atg2-PM4 mutation is likely to attenuate the primary lipid supply mechanism to such an extent that the cell compensates by engaging alternative lipid delivery pathways to the phagophore (Fig. 7B, right). In this context, we wish to emphasize that the observed rim-connected vesicle densities in our cryo-tomographic data represent cellular snapshots frozen in time. Based on these data

Journal of Cell Science (2026) 139, jcs265302. doi:10.1242/jcs.265302

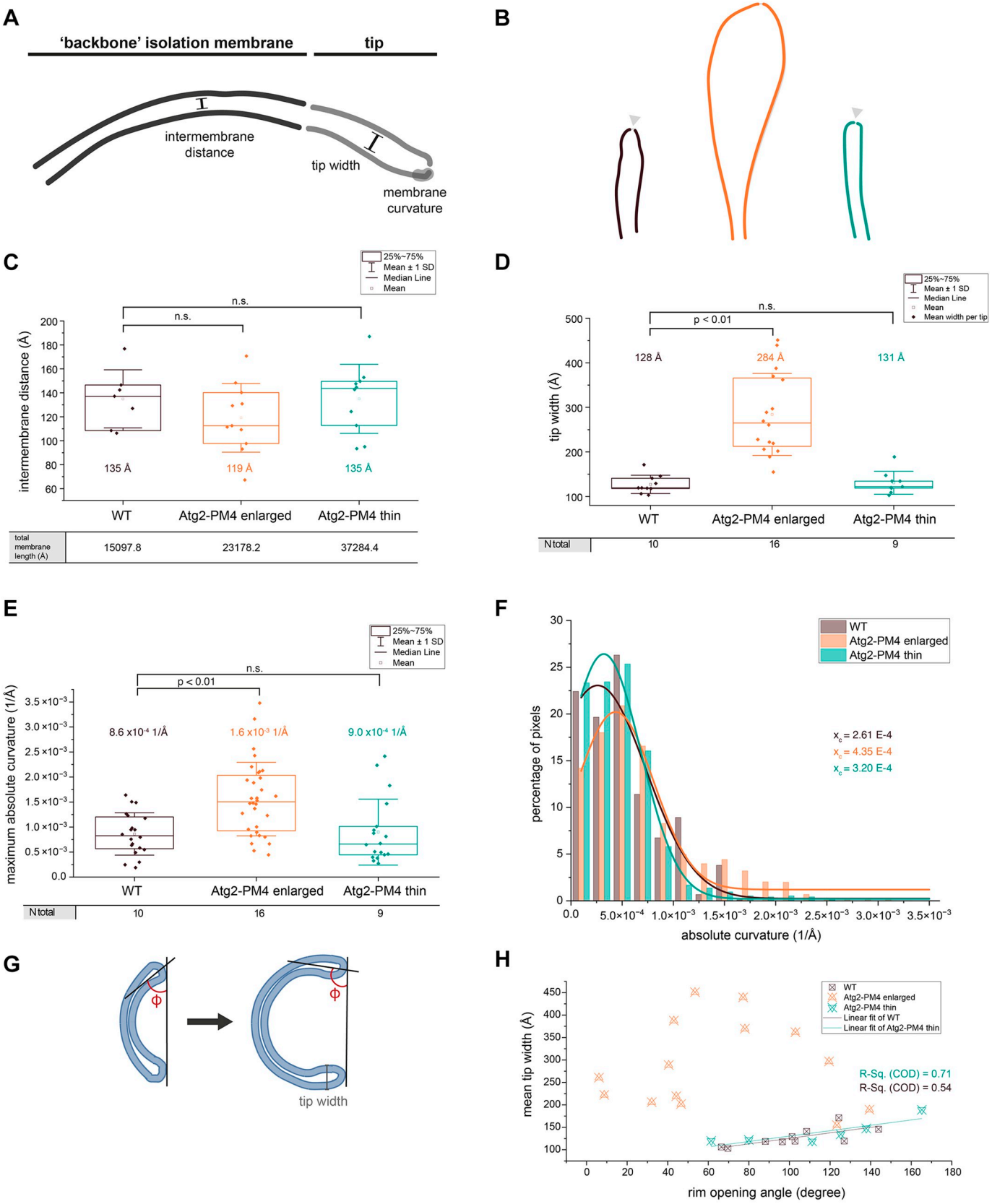


Fig. 5. See next page for legend.

Journal of Cell Science (2026) 139, jcs265302. doi:10.1242/jcs.265302

Fig. 5. Quantification of morphological features in phagophores. (A) Illustration of segmentation showing the analysed parts of phagophore morphology. Tip represents the two-dimensional section of the phagophore rim. (B) Diagrams of representative two-dimensional segmentations of the Atg2-WT (brown), Atg2-PM4 'enlarged' (orange) and Atg2-PM4 'thin' (green) through phagophore rim. Grey arrows indicate the utmost tip that was excluded from the curvature measurements. (C) Box plot comparing the intermembrane distance of 'backbone' phagophore between the Atg2-WT, Atg2-PM4 enlarged and Atg2-PM4 thin. (D) Box plot comparing mean phagophore tip width of all the segmented phagophores. (E) Box plot comparing the maximum absolute curvature of all the segmented phagophore tips across the Atg2-WT, Atg2-PM4 enlarged and Atg2 PM4-thin phenotype. Curvature of a given pixel was estimated by fitting a circle through the neighboring pixels 500 Å in each direction. The reciprocal radius of the best fitting circle is defined as the curvature. For more details, please refer to the Methods section. Custom box plots are shown in C–E, where the box represents the 25–75th percentiles, with the median (middle line) and mean (square) indicated. The whiskers show the 1 s.d. *n* values are given underneath. (F) Distribution of percentage of pixels of segmented phagophore tips across different absolute curvature values with Gauss curve fits. Note, due to the time-consuming nature of *in situ* cryo-ET, tomograms were not performed as independent replicates. (G) Schematic representation of the rim opening angle as proposed by (Bieber et al., 2022). (H) Relationship of rim opening angle and mean tip width (n=10, 14 and 9 for WT, Atg2-PM4 enlarged, Atg2-PM4 thin, respectively.). The R-square (coefficient of determination; COD) and the adjusted R-square values of the fitted curves are shown.

Table 3. Vesicle sizes and vesicle circularity

Vesicle Nr.	Diameter (nm)	Circularity
1	115	0.88
2	110	0.89
3	125	0.89
4	122	0.89
5	37	0.88
6	67	0.9
7	113	0.9
8	66	0.9
9	124	0.81
10	147	0.78
11	149	N/A
12	169	N/A
13	188	N/A
14	189	N/A
15	168	N/A

Circularity is defined here as $\frac{4\times\pi\times area}{circumference^2}$. Vesicle numbering as shown in Fig. S1.

alone, both directions of vesicle fusion and fission are possible to interpret. However, together with the characterization of the Atg2-PM4 mutant by live-cell imaging showing autophagy progression, although decelerated, we reason that when Atg2 lipid transfer is compromised, vesicle delivery by subsequent fusion with the phagophore contributing to expansion is more likely than vesicles budding off the phagophore rim.

Interestingly, the cellular origin of the observed vesicles could not be fully clarified. Apart from the established phagophore vicinity to the ER and lipid droplets, we could not identify any other cellular compartment associated with the vesicles. In the absence of experimental support, one could speculate that the observed vesicles might be Golgi-derived Atg9 vesicles (Yamamoto et al., 2012). However, most of the vesicles visualized here in cells were ∼90–180 nm in diameter, which is two- to three-fold larger than the previously reported size of 30–60 nm of isolated Atg9 vesicles (Yamamoto et al., 2012). These smaller vesicles have also been reported to be recruited by the Atg1 complex to the early PAS, where they form clusters or tubular structures acting as so called membrane seeds (Yamamoto et al., 2012; Mari et al., 2010; Feng et al., 2016; Papinski et al., 2014; Rao

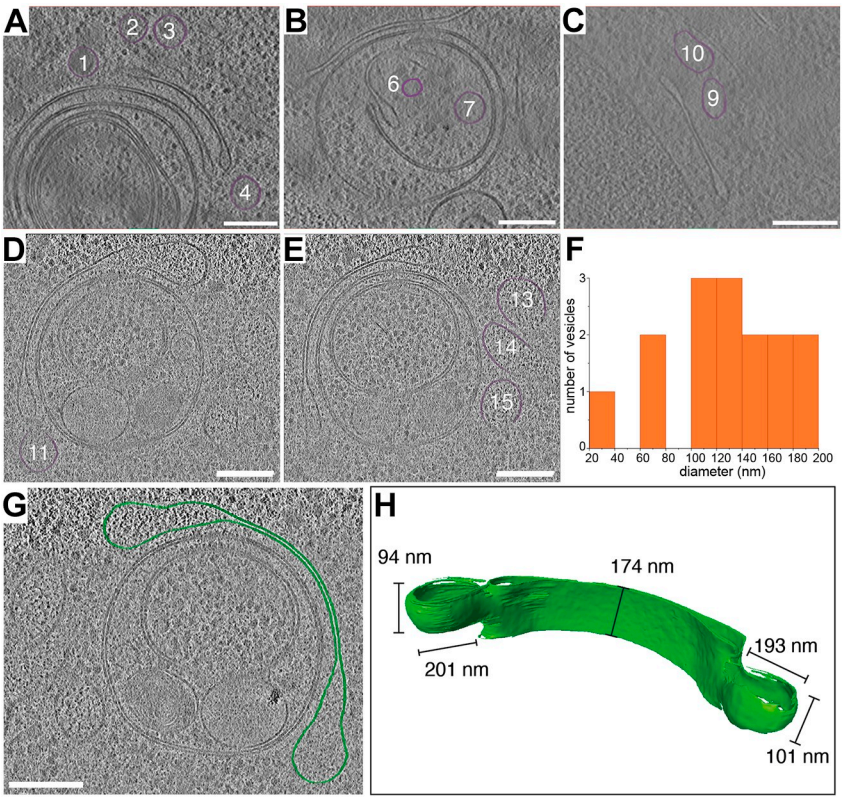


Fig. 6. Tomographic slices of phagophore rims in proximity to cytosolic vesicles in Atg2-PM4 cells. (A–E) Vesicles proximal to phagophore rims are presented in tomographic slices. (F) Size distribution of vesicles. Diameters and circularity values can be found in Table 3. Tomographic slices were denoised with IsoNet (Liu et al., 2022). (G) Tomographic slice with segmented phagophore (green). (H) Three-dimensional surface rendering of the phagophore in G with vesicles putatively fusing to the phagophore rims. Note, due to the time-consuming nature of *in situ* cryo-ET, tomograms were not performed in independent replicates. Scale bars: 200 nm.

Journal of Cell Science (2026) 139, jcs265302. doi:10.1242/jcs.265302

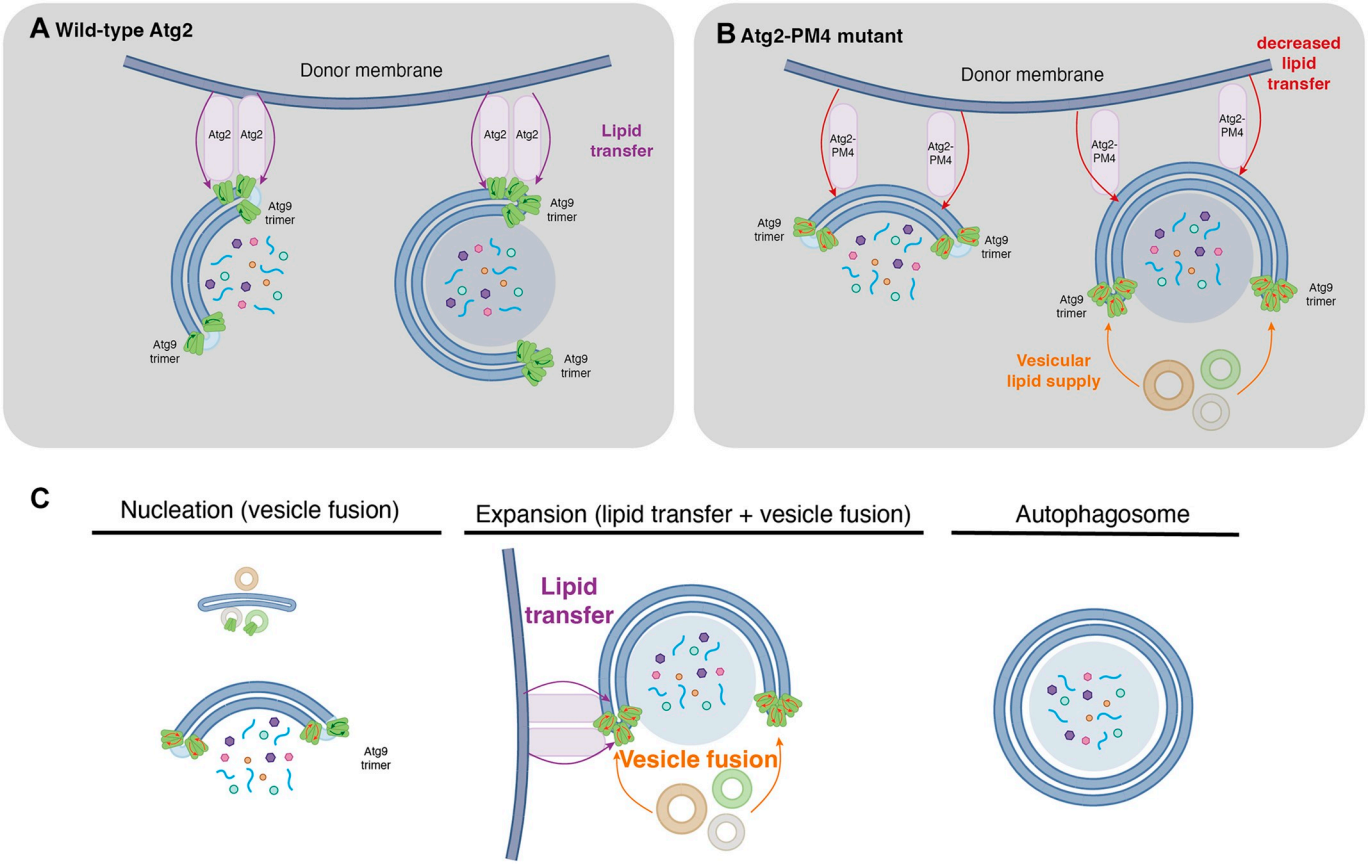


Fig. 7. Vesicle fusion can contribute to phagophore expansion. (A) Current phagophore expansion model in Atg2-WT cells. Atg2-WT spatially coupled with Atg9 is localized to the phagophore rim and transfers lipids (purple arrows) from the donor membrane to the phagophore rim. Atg9 transfers lipids to the inner leaflet of the phagophore membrane by its scramblase activity (dark green arrows). As a result of the Atg2–Atg9 lipid transfer-scramblase activities, the phagophore grows. (B) Proposed model of delayed phagophore expansion activity in Atg2-PM4 cells – through mislocalization of Atg2 (large red arrows) and decoupled Atg9 scramblase activity (small red arrows) growth of phagophore membrane is delayed. Cellular vesicles can provide additional lipids for its expansion (orange arrows). (C) During autophagosome biogenesis, small Atg9 vesicles fuse at the phagophore assembly site during early stages to form a nascent phagophore. Once the phagophore has established the corresponding membrane contact sites with the ER and/or ERES, the phagophore membrane expands by lipid transfer from the donor membrane and a possible contribution of vesicle fusion at the phagophore rims.

et al., 2016) rather than fusing to an expanding phagophore, as we believe to have visualized here (Fig. 7C). In mammalian systems, by contrast, ATG9A localizes in an ULK-1-independent manner during the nucleation step to autophagosome formation sites or omegasomes, which are subdomains of the ER providing a membrane platform to assemble on (Karanasios et al., 2016; Young et al., 2006). Furthermore, it has been shown that ATG9A cycles dynamically between endosomal compartments, the trans-Golgi network, the plasma membrane and phagophores, ATG9 vesicles only transiently associate with the growing phagophore, and ATG9 is not integrated into the isolation membrane (Orsi et al., 2012).

Our live-cell imaging data confirm that the observed vesicles are not derived from class E compartments and therefore not an artefact from the *snf7Δ* strain. Furthermore, our data are consistent with previous reports showing that Atg8 clusters do not overlap with class E compartments in *snf7Δ* as well as in *vps4Δ* ESCRT mutant cells, under both growing and nitrogen-starvation conditions (Zhou et al., 2019). The recent observation of membrane contact sites between the phagophore rim and the ERES mediated by the Atg2 and TRAPPIII complex (Gómez-Sánchez et al., 2025) might explain why COPII vesicles have been shown to colocalize with phagophore rims and have been identified as a membrane source previously (Graef et al., 2013; Shima et al., 2019; Suzuki et al., 2013). The diameters of canonical COPII vesicles are characterized as being in the size range of 60–80 nm (Kim et al., 2005), although they can also be significantly larger, up to 300 nm, in the presence of cargo (Gorur et al., 2017). The resolution and available details in the yeast tomograms were not sufficient to assign the nature of the vesicles neither for COPI nor clathrin lattices. Although the images reveal the vesicles are attached to the phagophore rims rather than the back of the phagophore, it remains open what the specific mechanisms behind vesicle trafficking to the phagophores and signals for vesicle–phagophore fusion are.

Regardless of our most striking observations on the phagophore morphology, we would also like to emphasize that about one-third of phagophore rims in the Atg2-PM4 phenotype had a width resembling that in the Atg2-WT, which could be explained by the presence of alternative lipid transporters, such as Vps13 or Csf1 (Dabrowski et al., 2023; Toulmay et al., 2022). Indeed, Vps13 has been shown to be a lipid transporter acting complementarily and non-rate limiting to Atg2 in autophagy (Dabrowski et al., 2023), possibly coordinated by a direct Atg9 interaction (Van Vliet et al., 2024). Csf1 has a putative length of 30 nm, which is consistent with the estimated lengths of densities observed tethering a phagophore

with the ER close to the phagophore rim (see Fig. 4H*, Table 2). Moreover, it has recently been shown that Csf1 localizes at ER–plasma membrane and ER–mitochondrial contact sites (Toulmay et al., 2022). Furthermore, Csf1 has been suggested to act as a lipid transfer protein in phosphatidyl ethanolamine metabolism and lipid homeostasis (Toulmay et al., 2022; John Peter et al., 2022). The occurrence of WT-like phagophore rims suggests that other lipid-transfer mechanisms exist that can take over some of the tasks typically performed by Atg2. Interestingly, we also observed a direct contact between lipid droplets and the phagophore, which have been described as lipid source for autophagosome biogenesis in yeast and mammalian cells (Dupont et al., 2014; Shpilka et al., 2015). To our knowledge, the direct transfer of phospholipids from the phospholipid monolayer on the surface of a lipid droplet to the phagophore in this way has not been observed so far by electron microscopy. Further studies are required to disentangle the contributions of the multiple players, such as Atg2, Vps13, Atg9 and Atg18, involved in the delivery of lipids to the growing phagophore.

Our tomographic observations suggest that vesicles are fusing with the rims of the phagophore rather than the sheet-like phagophore backbone. Given the high membrane curvature present at the phagophore rims, this geometry is likely to be favoured for membrane fusion with spherical cellular vesicles. According to EM observations of the Golgi, vesicles also primarily fuse with the rims rather the sheets (Donohoe et al., 2013). Together, our cryo-ET data recorded *in situ* reveal vesicle fusion at the stage of expanding phagophores and adds to the cellular repertoire of processes contributing to phagophore expansion.

MATERIALS AND METHODS

Yeast strains

The yeast strains used in this study are listed in Table S1. Genomic deletions were characterized with respect to expression and autophagic flux as shown in Fig. S4. Yeast genomic insertions and tagging were performed according to Janke et al. (Janke et al., 2004), and multiple deletions were generated by PCR knockout, mating and dissection. GFP–ATG8-containing strains were generated by crossing with yTB282 (*hi3Δ1 leu2Δ0 met15Δ ura3Δ0 atg8*::GFP-*ATG8*), which had been generated by seamless tagging (Khmelinskii et al., 2011). The genotype of generated strain was confirmed by colony PCR and western blot analysis.

For live-cell imaging of Vps8, Atg8 and the giant Ape1 assay, the *ATG2* and *SNF7* coding regions was replaced with the hygromycin-resistance gene (*hphNT1*) to create the *atg2Δ* strain, using PCR primers containing 60 bases of identity to the regions flanking the open reading frame (Janke et al., 2004). Gene knockout was verified by polymerase chain reaction (PCR) and Ape1-processing analysis (Mari et al., 2010). PCR-based integration of the mScarlet tag at the 3′ end of *VPS8* was used to generate a strain expressing C-terminal fusion protein under the control of the authentic promoter. The plasmid template for integration was pFA6-mScarlet-NatMX6 (Gómez-Sánchez et al., 2025).

For live-cell imaging of Atg2 and Atg8, *Δatg2::atg2^{PM4}-3xGFP-CaURA3* strains were generated by assembling the following fragments via gap repair into a pRS315 plasmid backbone: (1) a 1000 bp long region 5′-upstream of the endogenous *ATG2* locus, (2) full-length *atg2^{PM4}* C-terminally tagged with *3xGFP-CaURA3* derived from a pFA6a-*link-3yEGFP-CaURA3 plasmid*, and (4) a 1000 bp long region 3′-downstream of the endogenous *ATG2* locus. Following isolation, the plasmid was sequenced and enzymatically digested using the restriction enzymes *Spe*I and *Sal*I. Next, the cut plasmid fragment was transformed into pRS304-mCherry-*ATG8 Δatg19::His3MX6 Δatg2::NatMX6* cells. The Δ*atg2::Nat3MX6* cassette was replaced with the *atg2^{PM4}-3xGFP-CaUraMX6* construct via homologous recombination at the endogenous *ATG2* locus, resulting in the generation of pRS304-mCherry-*ATG8 Δatg19::His3MX6 Δatg2::atg2^{PM4}-3xGFP-CaURA3* cells.

Growth conditions

Strains were grown in rich (YPD) medium containing 1% yeast extract, 2% peptone (BD) and 2% glucose; or in synthetic drop-out medium (−Leu, −Ura, or −Leu−Ura, Formedium) supplemented with 2% glucose; or nitrogen starvation medium (SD-N) containing 0.17% yeast nitrogen base without amino acids or ammonium sulfate (Thermo Fisher Scientific) and 2% glucose to mid-log phase. Pre-cultures (10 ml) for vitrification in either YPD or synthetic drop-out medium were inoculated with a single colony. Cells were cultured at 30°C for at least 14 h to ensure cells would not be stressed. The optical density at 600 nm (OD_{600}) was monitored, and as soon as it was between 0.55 and 0.8 the culture was used for starvation and plunge freezing. For nitrogen starvation, the cells were pelleted at 3000 ***g*** for 5 min and washed three times with SD-N medium. Cells were incubated in SD-N medium for a minimum of 2 h and a maximum of 5 h before vitrification.

Yeast cell transformation

Plasmids used in this work are listed in Table S2. Transformation procedures are described in Gietz (2014) as the ‘Quick and Easy Transformation Protocol’ with minor modifications also known as the LiAc/SS Carrier DNA/PEG method. In brief, the transformation buffer was prepared in advance with 0.24 M lithium acetate and 47% PEG 3350 (sterile filtered, Sigma-Aldrich). The reaction mix was composed of 5 µl single stranded salmon sperm carrier DNA (Sigma-Aldrich), 85 µl transformation buffer, 10 µl 1 M DTT and 0.5 to 2 µl of the plasmid (300 to 500 ng/µl concentration). The yeast patch was scraped off the agar with a sterile loop and mixed into the transformation reaction mix directly. This suspension was very briefly vortexed and incubated at 45°C for exactly 30 min. Finally, the reaction mix was plated out on the appropriate selection agar plate.

Detection of expression and autophagy flux

Yeast cell cultures were precipitated with 7% trichloroacetic acid (TCA) for 30 min on ice. Precipitated proteins were pelleted at 16,000 ***g*** for 15 min at 4°C, washed with 1 ml acetone, air-dried, resuspended in urea loading buffer (120 mM Tris-HCl pH 6.8, 5% glycerol, 8 M urea, 143 mM β-mercaptoethanol, 8% SDS), boiled and analysed by SDS-PAGE followed by immunoblotting.

Antibodies

The following antibodies were used in this study: rabbit polyclonal anti-*SNF7* (1:5000, David Teis, Medical University Innsbruck, Austria), rabbit polyclonal anti-Ape1 [1:15,000, generated by immunizing rabbits with a synthetic peptide corresponding to amino acids 168-182 (Papinski et al., 2014)] and mouse monoclonal anti-RFP (1:1000, 6g6, Ref No. 6g6-100 Lot No51020014AB-05, Chromotek).

Live-cell fluorescence microscopy

To examine bulk autophagy via imaging of Vps8 and Atg8, cells were grown in SD-URA medium before transferring them to SD-N medium for 2 h. Cells were incubated with CellTracker™ Blue 7-amino-4-chloromethylcoumarin dye (CMAC, Thermo Fisher Scientific, C2110) as previously described (Stefan and Blumer, 1999) for 10 min to stain the vacuolar lumen. Images were acquired with a DeltaVision Elite RT microscope system (GE Healthcare, Applied Precision), equipped with a UPLASPO 100× oil/1.40 NA objective, a pco.edge 5.5 sCMOS camera (PCO) and a seven-colour InsightSSI solid-state illumination system (GE Healthcare, Applied Precision). Images were generated by collecting a Z-stack of 22 pictures with focal planes 0.20 µm apart to cover the entire volume of a yeast cell, and subsequently deconvolved using the SoftWoRx software (Applied Precision). A single focal plane is shown in the figures. The percentage of Atg8-positive structures associated with the Vps8 clusters was determined by analysing 50 cells from three independent experiments. Data represent the average of three independent biological replicates as mean±s.d. The shown data are those of a representative experiment. Data were statistically analysed with GraphPad Prism 6 (GraphPad Software Inc.), using a two-tailed unpaired *t*-test with Welch’s correction. All comparisons with $P<0.05$ were considered statistically significant and indicated with a single asterisk.

For imaging of Atg2 and Atg8, *S. cerevisiae* cells were imaged at room temperature after 1 h of nitrogen starvation in 96-well glass-bottom microplates (Greiner Bio-One). Live-cell images and semi-three-dimensional time-lapse fluorescence images were taken using a Dragonfly 500 spinning disk microscope (Andor) attached to an inverted Ti2 microscope stand (Nikon) with a CFI Plan Apo Lambda 60×/1.4 oil immersion objective (Nikon) and a Zyla 4.2 sCMOS camera (Andor). Following acquisition, images were processed using Fiji software (version 2.1.0). The number of Atg8 puncta and expanded autophagosomal membranes, including expanded tubular and ring-shaped structures was analysed after 1 h of nitrogen starvation, by randomly marking 50 cells with the Fiji multipoint tool.

To induce giant Ape1 oligomers formation bulk autophagy, cells expressing the pDP105 plasmid were grown to exponential phase in synthetic minimal medium containing 250 µM of $CuSO_4$ before being treated with 400 ng/ml rapamycin (LC Laboratories) for 3 h (Gómez-Sánchez et al., 2018). Images were acquired with a DeltaVision Elite RT microscope system (GE Healthcare, Applied Precision), equipped with a UPLASPO 100× oil/1.40 NA objective, a pco.edge 5.5 sCMOS camera (PCO) and a seven-colour InsightSSI solid-state illumination system (GE Healthcare, Applied Precision). Images were generated by collecting a *Z*-stack of 22 pictures with focal planes 0.20 µm apart to cover the entire volume of a yeast cell, and subsequently deconvolved using the SoftWoRx software (Applied Precision). For figure preparation, Photoshop CC and Illustrator CC software (Adobe) were used. A single focal plane is shown in the figures. Distribution of fluorescent Atg9 chimera on the phagophore was investigated by counting ≥20 cells from three independent experiments. Recorded data represent the average of three independent biological replicates as mean±s.d. The shown data are those of a representative experiment. Data were statistically analysed with GraphPad Prism 10 (GraphPad Software Inc.), using a two-tailed unpaired *t*-test with Welch's correction. All comparisons with a $P<0.05$ were considered statistically significant and indicated with asterisks.

Cell vitrification

Nitrogen starved *S. cerevisiae* cells were applied to Quantifoil (Großlöbichau, Germany) grids (Cu 200 mesh, R2/1, either carbon or SiO_2 film). In some cases, carboxylate-modified microspheres (1 µm diameter crimson or 1 µm diameter blue, Invitrogen, Thermo Fisher Scientific, Waltham, MA, USA) were added to the cell suspension prior to plunge freezing. Cells were vitrified using a liquid ethane and propane mixture or liquid ethane at liquid nitrogen temperature and a Vitrobot Mark IV (Thermo Fisher Scientific). Back-side blotting was carried out by covering the paddle of the device on the side of the grid film with a Teflon disc (generous donation from Dr Julia Mahamid, Molecular Systems Biology, European Molecular Biology Laboratory, Heidelberg, Germany). The paddle at the back side of the grid was covered with filter paper (Whatman 597, Maidstone, UK) as standard. For a given grid, 7 µl of cell suspension were applied and after 1 s wait time excess liquid was blotted away. The blot time ranged from 10 to 13 s. Blot force was kept consistently at −10, chamber humidity at 80% and chamber temperature at 30°C. After plunge-freezing the grids, they were usually clipped into autogrids (Thermo Fisher Scientific) for further electron microscopy applications.

Lamella preparation

For this work, the Aquilos 2 dual-beam FIB microscope (Thermo Fisher Scientific) was used. Grids were kept at approximately −195°C during the entire milling procedure. FIB-milling procedures were carried out as described in Schaffer et al. (2017) with some modifications. Lamella were milled using the gallium beam at 30 kV (0.1 nA to 10 pA) with a typical milling angle of 10° (i.e. stage angle of 17°). After setting eucentric height at the sites of interest, the grids were sputter-coated with platinum (30 mA, 0.1 mbar) for 15 s, then coated with an organometallic platinum layer using the gas injection system (GIS) for 90 to 105 s. Subsequently, another sputter-coating layer was applied (30 mA, 0.1 mbar) for 15 s. Most of the milling sessions were carried out using the automated milling software AutoTEM (Thermo Fisher Scientific), followed by manual polishing. Once the lamellae were at their final thickness, in some cases a final sputter coat was applied (30 mA, 0.1 mbar) for three seconds. Lamellae were imaged on the retro-fitted Meteor (Delmic BV, Delft, NL) bright-field cryo-fluorescence microscope with a 50×0.5 NA (Olympus LMPLFLN WD 10.6 mm) objective. The samples were kept at approximately −195°C on the stage of the Aquilos 2 during measurements. Except for one tomogram (Fig. 1I), all tomographic data was collected based on FM-TEM correlation from images collected with the Meteor.

Cryo-electron tomography

After preparation and fluorescent imaging of the lamellae, the grids were transferred to the following transmission electron microscopes: a Talos Arctica (200 keV, Thermo Fisher Scientific) microscope together with a K3 direct electron detector with Quantum GIF filter (Gatan Inc., Pleasanton, CA, USA) and Titan Krios (300 keV, Thermo Fisher Scientific) equipped with a Falcon 4 direct electron detector (Thermo Fisher Scientific). In both cases, cameras were operated in movie mode with 10 to 15 frames per movie. For data collection and correlation of TEM overview images with fluorescence data on the Talos Arctica, the software package SerialEM (Mastronarde, 2003) was used. For acquisition of lamella overview images and correlation with fluorescence data on the Titan Krios, the Maps software (Thermo Fisher Scientific) was utilized. For automated acquisition of tilt series on the Titan Krios, the Tomography software (Thermo Fisher Scientific) was used. Tilt series were acquired using the dose–symmetric acquisition scheme (Hagen et al., 2017) implemented in both SerialEM and Tomography over an angular range of −60° to +60° with 2° increments. The set defocus was −5 µm and cumulative dose was kept below 130 $e^{-}/Å^2$. The pixel size ranged from 1.74 to 2.78 Å depending on the camera and camera operation mode. Only four tilt series were collected on the Titan Krios; these were tilt series of the Atg2-WT of which two tomographic slices are shown in Fig. 3F–I. All other tomographic data analysed in this manuscript were acquired on the Talos Arctica.

Tomographic image processing

For the tomographic data processing and analysis workflow, acquired tilt frames were preprocessed using WARP (Tegunov and Cramer, 2019). Patch-tracking guided tilt series alignment and tomogram reconstruction based on weighted back projection was done with IMOD (Mastronarde, 1997; Kremer et al., 1996) or AreTomo (Zheng et al., 2022). Denoising and missing wedge correction were carried out with the help of IsoNet (Liu et al., 2022). Segmentation was done with MemBrain v2 (Lamm et al., 2026) (an updated version from MemBrain; Lamm et al., 2022) using its pretrained model (Version b from 10th Aug 2023) on the non-denoised data. Segmentations were subsequently manually corrected and completed using Dragonfly software, Version 2022.2 (Comet Technologies Canada Inc.).

The data evaluation and quantification of the presented tomograms were carried out on tomographic slices in 2D with the help of CryoVIA (Schönnenbeck et al., 2025). Segmentations of regions of interest were manually separated into an inner and outer bilayer omitting the tips, saved to individual .tif files and input into the toolkit. Prior to curvature measurements, a Gaussian filter (window size of 9 and sigma of 4) was applied in order to avoid overfitting curvature inaccuracies due to small errors in the segmentation. Subsequently a single pixel-wide skeleton of the membrane was generated. For each pixel of this skeleton, the curvature was determined by selecting the neighbouring pixels in each direction along the skeleton up to 500 Å away from the pixel of interest. Next, a circle with the best possible fit through these pixels was generated. The inverse of this circle's radius was defined as the curvature of the pixel of interest. For distance measurements, the single-pixel skeleton was also used. A support vector machine was used to determine a line separating the two sides of the segmented rim sections, (i.e. tips). The length of perpendicular lines (relative to the separation line) connecting individual pixels of each side of the tip were then determined and defined as the distance between the given two pixels. Circularity is defined here as $\frac{4\times\pi\times area}{\text{circumference}^2}$. Circularity of vesicles could only be determined for vesicles where the segmentation was complete and had no gaps, as the area was otherwise not clearly defined. Data analysis and plotting were carried out in Origin(Pro) 2023 (Version 10.0.0.154, OriginLab Corporation, Northampton, MA, USA).

Illustrations and figures

Fluorescence images from the Meteor bright-field cryo-fluorescence microscope were generated using the proprietary software Odemis (Delmic BV, Delft, NL). Figures of tomograms were made using IMOD (Kremer et al., 1996) and Dragonfly software, Version 2022.2 (Comet Technologies Canada Inc.). For live-cell imaging figure preparation, Fiji, Photoshop CC and Illustrator CC software (Adobe) were used. Some of the structural biology software used in this work, such as IMOD, AreTomo, IsoNet, and PyMOL was compiled and configured by SBGrid (Morin et al., 2013).

Acknowledgements

We gratefully acknowledge the electron microscopy training, imaging and access time granted by the life science EM facility of the Ernst-Ruska Centre at Forschungszentrum Jülich. We thank Dr Julio Ortiz for SerialEM training and support in setting up the SerialEM imaging settings. We also thank David Kartte for his help in setting up processing software and segmentation training. We thank Prof. Fulvio Reggiori (Department of Biomedicine, Aarhus University, Denmark) for reagents. The authors gratefully acknowledge the computing time granted by the JARA Vergabegremium and provided on the JARA Partition part of the supercomputer JURECA at Forschungszentrum Jülich (Thörnig, 2021).

Competing interests

The authors declare no competing or financial interests.

Author contributions

Conceptualization: C.S., C.O.d.P.N., M.L., C.K.; Data curation: C.S., C.O.d.P.N., R.G.-S., R.D., M.G.; Formal analysis: C.S., C.O.d.P.N., R.D., M.G., R.G.-S., P.S., M.L. ; Funding acquisition: C.S., R.G.-S., M.G., K.C.; Investigation: C.S., C.O.d.P.N., M.L., R.D., R.G.-S., M.G., C.K.; Methodology: C.S., C.O.d.P.N., M.L., R.D., R.G.-S., S.B., P.S., M.G., C.K.; Resources: C.S., C.K., M.G.; Software: P.S.; Supervision: C.S., M.G., C.K.; Validation: C.S., C.O.d.P.N., M.L., C.K.; Visualization: C.S., C.O.d.P.N., R.D., R.G.-S.; Writing – original draft: C.S., C.O.d.P.N.; Writing – review & editing: C.S., C.O.d.P.N., M.L., R.D., R.G.-S., S.B., M.G., C.K.

Funding

The authors acknowledge financial support through Gravitation grant 'FLOW' (024.006.036) from the Dutch Ministry of Education, Culture, and Science (OCW; Ministerie van Onderwijs, Cultuur en Wetenschap) (R.G.-S.). The Kraft laboratory has received funding from the Deutsche Forschungsgemeinschaft (DFG, German Research Foundation) Project-ID 450216812, Project ID 409673687, SFB 1381 (Project ID 403222702), under Germany's Excellence Strategy (CIBSS - EXC-2189- Project ID 390939984), from the European Research Council (ERC) under the European Union's Horizon 2020 research and innovation programme under grant agreement No. 769065. C.S. acknowledges funding from the European Research Council within the Horizon Europe innovation funding programme under Grant Agreement 101118656 (ERC Synergy project 4D-BioSTEM). This work reflects only the authors' view and the European Union's Horizon 2020 research and innovation programme is not responsible for any use that may be made of the information it contains. Open Access funding provided by Helmholtz Association, Germany. Deposited in PMC for immediate release.

Data and resource availability

Selected tomograms have been deposited to EMDB (https://www.ebi.ac.uk/emdb/). Tomograms shown in Fig. 2G and J are available through accession number EMD-57825 and EMD-57824, respectively. Tomograms shown in Fig. 3D,E, and I are available through accession number EMD-57827, EMD-57823 and EMD-57826, respectively. The remaining data is available upon request to the corresponding author. All other relevant data and details of resources can be found within the article and its supplementary information.

First Person

This article has an associated First Person interview with the first author of the paper.

Special Issue

This article is part of the Special Issue 'Imaging Cell Architecture and Dynamics', guest edited by Francesca Bottanelli and Giulia Zanetti. See related articles at https://journals.biologists.com/jcs/issue/139/21.

References

Axe, E. L., Walker, S. A., Manifava, M., Chandra, P., Roderick, H. L., Habermann, A., Griffiths, G. and Ktistakis, N. T. (2008). Autophagosome formation from membrane compartments enriched in phosphatidylinositol 3-phosphate and dynamically connected to the endoplasmic reticulum. *J. Cell Biol.* **182**, 685-701. doi:10.1083/jcb.200803137

Berkamp, S., Smeets, M., Caignard, A., Jani, R., Daviran, D. and Sachse, C. (2023). High-throughput correlative light and cryo-electron microscopy pipeline using PRIMO micropatterning, CERES ice shield and the METEOR In-chamber fluorescence light microscope. *Microsc. Microanal.* **29**, 1027-1028. doi:10.1093/micmic/ozad067.521

Berkamp, S., Jungbluth, L., Katranidis, A., Mostafavi, S., Korculanin, O., Lu, P.-H., Ickert, L., Dierig, M. M., Sharma, L., Thukral, L. et al. (2025). Structural organization of p62 filaments and the cellular ultrastructure of calcium-rich p62-enwrapped lipid droplet cargo. *Nat. Commun.* **16**, 10810. doi:10.1038/s41467-025-66785-7

Bieber, A., Capitanio, C., Erdmann, P. S., Fiedler, F., Beck, F., Lee, C.-W., Li, D., Hummer, G., Schulman, B. A., Baumeister, W. et al. (2022). In situ structural analysis reveals membrane shape transitions during autophagosome formation. *Proc. Natl. Acad. Sci. USA* **119**, e2209823119. doi:10.1073/pnas.2209823119

Broadbent, D. G., Barnaba, C., Perez, G. I. and Schmidt, J. C. (2023). Quantitative analysis of autophagy reveals the role of ATG9 and ATG2 in autophagosome formation. *J. Cell Biol.* **222**, e202210078. doi:10.1083/jcb.202210078

Bykov, Y. S., Schaffer, M., Dodonova, S. O., Albert, S., Plitzko, J. M., Baumeister, W., Engel, B. D. and Briggs, J. A. (2017). The structure of the COPI coat determined within the cell. *eLife* **6**, e32493. doi:10.7554/eLife.32493

Cabezudo, A. C., Holzer, E., Martens, S. and Hummer, G. (2025). Pathway and gates for ATG2A-mediated lipid transport in autophagy. *bioRxiv*. doi:10.1101/2025.11.16.688672

Capitanio, C., Bieber, A. and Wilfling, F. (2023). How membrane contact sites shape the phagophore. *Contact* **6**, 25152564231162495. doi:10.1177/25152564231162495

Cheng, Y., Boll, W., Kirchhausen, T., Harrison, S. C. and Walz, T. (2007). Cryo-electron tomography of clathrin-coated vesicles: structural implications for coat assembly. *J. Mol. Biol.* **365**, 892-899. doi:10.1016/j.jmb.2006.10.036

Cheng, J., Fujita, A., Yamamoto, H., Tatematsu, T., Kakuta, S., Obara, K., Ohsumi, Y. and Fujimoto, T. (2014). Yeast and mammalian autophagosomes exhibit distinct phosphatidylinositol 3-phosphate asymmetries. *Nat. Commun.* **5**, 3207. doi:10.1038/ncomms4207

Chowdhury, S., Otomo, C., Leitner, A., Ohashi, K., Aebersold, R., Lander, G. C. and Otomo, T. (2018). Insights into autophagosome biogenesis from structural and biochemical analyses of the ATG2A-WIPI4 complex. *Proc. Natl. Acad. Sci. USA* **115**, E9792-E9801. doi:10.1073/pnas.1811874115

Chumpen Ramirez, S., Gómez-Sánchez, R., Verlhac, P., Hardenberg, R., Margheritis, E., Cosentino, K., Reggiori, F. and Ungermann, C. (2023). Atg9 interactions via its transmembrane domains are required for phagophore expansion during autophagy. *Autophagy* **19**, 1459-1478. doi:10.1080/15548627.2022.2136340

Ciuffa, R., Lamark, T., Tarafder, A. K., Guesdon, A., Rybina, S., Hagen, W. J. H., Johansen, T. and Sachse, C. (2015). The selective autophagy receptor p62 forms a flexible filamentous helical scaffold. *Cell Rep.* **11**, 748-758. doi:10.1016/j.celrep.2015.03.062

Dabrowski, R., Tulli, S. and Graef, M. (2023). Parallel phospholipid transfer by Vps13 and Atg2 determines autophagosome biogenesis dynamics. *J. Cell Biol.* **222**, e202211039. doi:10.1083/jcb.202211039

De, M., Oleskie, A. N., Ayyash, M., Dutta, S., Mancour, L., Abazeed, M. E., Brace, E. J., Skiniotis, G. and Fuller, R. S. (2017). The Vps13p–Cdc31p complex is directly required for TGN late endosome transport and TGN homotypic fusion. *J. Cell Biol.* **216**, 425-439. doi:10.1083/jcb.201606078

Donohoe, B. S., Kang, B., Gerl, M. J., Gergely, Z. R., McMichael, C. M., Bednarek, S. Y. and Staehelin, L. A. (2013). *Cis* –Golgi Cisternal assembly and biosynthetic activation occur sequentially in plants and algae. *Traffic* **14**, 551-567. doi:10.1111/tra.12052

Dupont, N., Chauhan, S., Arko-Mensah, J., Castillo, E. F., Masedunskas, A., Weigert, R., Robenek, H., Proikas-Cezanne, T. and Deretic, V. (2014). Neutral lipid stores and lipase PNPLA5 contribute to autophagosome biogenesis. *Curr. Biol.* **24**, 609-620. doi:10.1016/j.cub.2014.02.008

Feng, Y., Backues, S. K., Baba, M., Heo, J.-M., Harper, J. W. and Klionsky, D. J. (2016). Phosphorylation of Atg9 regulates movement to the phagophore assembly site and the rate of autophagosome formation. *Autophagy* **12**, 648-658. doi:10.1080/15548627.2016.1157237

Förster, F. and Briegel, A. (Eds.) (2024). *Cryo-Electron Tomography: Structural Biology in situ, Focus on Structural Biology*. Cham: Springer International Publishing. doi:10.1007/978-3-031-51171-4

Frolov, V. A., Shnyrova, A. V. and Zimmerberg, J. (2011). Lipid polymorphisms and membrane shape. *Cold Spring Harb. Perspect. Biol.* **3**, a004747. doi:10.1101/cshperspect.a004747

Fujioka, Y., Alam, J. M., Noshiro, D., Mouri, K., Ando, T., Okada, Y., May, A. I., Knorr, R. L., Suzuki, K., Ohsumi, Y. et al. (2020). Phase separation organizes the site of autophagosome formation. *Nature* **578**, 301-305. doi:10.1038/s41586-020-1977-6

Ge, L., Melville, D., Zhang, M. and Schekman, R. (2013). The ER–Golgi intermediate compartment is a key membrane source for the LC3 lipidation step of autophagosome biogenesis. *eLife* **2**, e00947. doi:10.7554/eLife.00947

Ge, L., Zhang, M. and Schekman, R. (2014). Phosphatidylinositol 3-kinase and COPII generate LC3 lipidation vesicles from the ER-Golgi intermediate compartment. *eLife* **3**, e04135. doi:10.7554/eLife.04135

Ghanbarpour, A., Valverde, D. P., Melia, T. J. and Reinisch, K. M. (2021). A model for a partnership of lipid transfer proteins and scramblases in membrane expansion and organelle biogenesis. *Proc. Natl. Acad. Sci. USA* **118**, e2101562118. doi:10.1073/pnas.2101562118

Gietz, R. D. (2014). Yeast transformation by the LiAc/SS Carrier DNA/PEG method. In *Yeast Genetics* (ed. J. S. Smith and D. J. Burke), pp. 1-12. New York, NY: Springer New York. doi:10.1007/978-1-4939-1363-3_1

Gómez-Sánchez, R., Rose, J., Guimarães, R., Mari, M., Papinski, D., Rieter, E., Geerts, W. J., Hardenberg, R., Kraft, C., Ungermann, C. et al. (2018). Atg9 establishes Atg2-dependent contact sites between the endoplasmic reticulum and phagophores. *J. Cell Biol.* **217**, 2743-2763. doi:10.1083/jcb.201710116

Gómez-Sánchez, R., Chumpen Ramirez, S., Vargas Duarte, P., Hu, Y., Mari, M., Olschewski, K., Hardenberg, R., Fromme, J. C., Ungermann, C. and Reggiori, F. (2025). Establishment of the phagophore–ERES membrane contact site initiates phagophore elongation. *Nat. Struct. Mol. Biol.* **32**, 2319-2334. doi:10.1038/s41594-025-01621-6

Gorur, A., Yuan, L., Kenny, S. J., Baba, S., Xu, K. and Schekman, R. (2017). COPII-coated membranes function as transport carriers of intracellular procollagen I. *J. Cell Biol.* **216**, 1745-1759. doi:10.1083/jcb.201702135

Graef, M., Friedman, J. R., Graham, C., Babu, M. and Nunnari, J. (2013). ER exit sites are physical and functional core autophagosome biogenesis components. *Mol. Biol. Cell* **24**, 2918-2931. doi:10.1091/mbc.e13-07-0381

Hagen, W. J. H., Wan, W. and Briggs, J. A. G. (2017). Implementation of a cryo-electron tomography tilt-scheme optimized for high resolution subtomogram averaging. *J. Struct. Biol.* **197**, 191-198. doi:10.1016/j.jsb.2016.06.007

Hailey, D. W., Rambold, A. S., Satpute-Krishnan, P., Mitra, K., Sougrat, R., Kim, P. K. and Lippincott-Schwartz, J. (2010). Mitochondria supply membranes for autophagosome biogenesis during starvation. *Cell* **141**, 656-667. doi:10.1016/j.cell.2010.04.009

Hamasaki, M., Furuta, N., Matsuda, A., Nezu, A., Yamamoto, A., Fujita, N., Oomori, H., Noda, T., Haraguchi, T., Hiraoka, Y. et al. (2013). Autophagosomes form at ER–mitochondria contact sites. *Nature* **495**, 389-393. doi:10.1038/nature11910

Hanada, T., Noda, N. N., Satomi, Y., Ichimura, Y., Fujioka, Y., Takao, T., Inagaki, F. and Ohsumi, Y. (2007). The Atg12-Atg5 conjugate has a novel E3-like activity for protein lipidation in autophagy. *J. Biol. Chem.* **282**, 37298-37302. doi:10.1074/jbc.C700195200

Hayashi-Nishino, M., Fujita, N., Noda, T., Yamaguchi, A., Yoshimori, T. and Yamamoto, A. (2009). A subdomain of the endoplasmic reticulum forms a cradle for autophagosome formation. *Nat. Cell Biol.* **11**, 1433-1437. doi:10.1038/ncb1991

Hollenstein, D. M., Gómez-Sánchez, R., Ciftci, A., Kriegenburg, F., Mari, M., Torggler, R., Licheva, M., Reggiori, F. and Kraft, C. (2019). Vac8 spatially confines autophagosome formation at the vacuole in S. *cerevisiae*. *J. Cell Sci.* **132**, jcs235002. doi:10.1242/jcs.235002

Jakobi, A. J., Huber, S. T., Mortensen, S. A., Schultz, S. W., Palara, A., Kuhm, T., Shrestha, B. K., Lamark, T., Hagen, W. J. H., Wilmanns, M. et al. (2020). Structural basis of p62/SQSTM1 helical filaments and their role in cellular cargo uptake. *Nat. Commun.* **11**, 440. doi:10.1038/s41467-020-14343-8

Janke, C., Magiera, M. M., Rathfelder, N., Taxis, C., Reber, S., Maekawa, H., Moreno–Borchart, A., Doenges, G., Schwob, E., Schiebel, E. et al. (2004). A versatile toolbox for PCR–based tagging of yeast genes: new fluorescent proteins, more markers and promoter substitution cassettes. *Yeast* **21**, 947-962. doi:10.1002/yea.1142

John Peter, A. T., van Schie, S. N. S., Cheung, N. J., Michel, A. H., Peter, M. and Kornmann, B. (2022). Rewiring phospholipid biosynthesis reveals resilience to membrane perturbations and uncovers regulators of lipid homeostasis. *EMBO J.* **41**, e109998. doi:10.15252/embj.2021109998

Karanasios, E., Walker, S. A., Okkenhaug, H., Manifava, M., Hummel, E., Zimmermann, H., Ahmed, Q., Domart, M.-C., Collinson, L. and Ktistakis, N. T. (2016). Autophagy initiation by ULK complex assembly on ER tubulovesicular regions marked by ATG9 vesicles. *Nat. Commun.* **7**, 12420. doi:10.1038/ncomms12420

Kawabata, T. and Yoshimori, T. (2020). Autophagosome biogenesis and human health. *Cell Discov.* **6**, 33. doi:10.1038/s41421-020-0166-y

Khmelinskii, A., Meurer, M., Duishoev, N., Delhomme, N. and Knop, M. (2011). Seamless gene tagging by endonuclease-driven homologous recombination. *PLoS ONE* **6**, e23794. doi:10.1371/journal.pone.0023794

Kim, J., Huang, W.-P. and Klionsky, D. J. (2001). Membrane recruitment of Aut7p in the autophagy and cytoplasm to vacuole targeting pathways requires Aut1p, Aut2p, and the autophagy conjugation complex. *J. Cell Biol.* **152**, 51-64. doi:10.1083/jcb.152.1.51

Kim, J., Hamamoto, S., Ravazzola, M., Orci, L. and Schekman, R. (2005). Uncoupled packaging of amyloid precursor protein and presenilin 1 into coat protein complex II vesicles. *J. Biol. Chem.* **280**, 7758-7768. doi:10.1074/jbc.M411091200

Kotani, T., Kirisako, H., Koizumi, M., Ohsumi, Y. and Nakatogawa, H. (2018). The Atg2-Atg18 complex tethers pre-autophagosomal membranes to the endoplasmic reticulum for autophagosome formation. *Proc. Natl. Acad. Sci.* **115**, 10363-10368. doi:10.1073/pnas.1806727115

Kremer, J. R., Mastronarde, D. N. and McIntosh, J. R. (1996). Computer visualization of three-dimensional image data using IMOD. *J. Struct. Biol.* **116**, 71-76. doi:10.1006/jsbi.1996.0013

Lamm, L., Righetto, R. D., Wietrzynski, W., Pöge, M., Martinez-Sanchez, A., Peng, T. and Engel, B. D. (2022). MemBrain: a deep learning-aided pipeline for detection of membrane proteins in Cryo-electron tomograms. *Comput. Methods Programs Biomed.* **224**, 106990. doi:10.1016/j.cmpb.2022.106990

Lamm, L., Zufferey, S., Zhang, H., Righetto, R. D., Waltz, F., Wietrzynski, W., Yamauchi, K. A., Burt, A., Liu, Y., Martinez-Sanchez, A. et al. (2026). MemBrain v2: an end-to-end tool for the analysis of membranes in cryo-electron tomography. *Nat. Methods*, 1-10. doi:10.1038/s41592-026-03178-8

Li, M., Tripathi-Giesgen, I., Schulman, B. A., Baumeister, W. and Wilfling, F. (2023). In situ snapshots along a mammalian selective autophagy pathway. *Proc. Natl. Acad. Sci. USA* **120**, e2221712120. doi:10.1073/pnas.2221712120

Liu, Y.-T., Zhang, H., Wang, H., Tao, C.-L., Bi, G.-Q. and Zhou, Z. H. (2022). Isotropic reconstruction for electron tomography with deep learning. *Nat. Commun.* **13**, 6482. doi:10.1038/s41467-022-33957-8

Longatti, A., Lamb, C. A., Razi, M., Yoshimura, S., Barr, F. A. and Tooze, S. A. (2012). TBC1D14 regulates autophagosome formation via Rab11- and ULK1-positive recycling endosomes. *J. Cell Biol.* **197**, 659-675. doi:10.1083/jcb.201111079

Maeda, S., Otomo, C. and Otomo, T. (2019). The autophagic membrane tether ATG2A transfers lipids between membranes. *eLife* **8**, e45777. doi:10.7554/eLife.45777

Maeda, S., Yamamoto, H., Kinch, L. N., Garza, C. M., Takahashi, S., Otomo, C., Grishin, N. V., Forli, S., Mizushima, N. and Otomo, T. (2020). Structure, lipid scrambling activity and role in autophagosome formation of ATG9A. *Nat. Struct. Mol. Biol.* **27**, 1194-1201. doi:10.1038/s41594-020-00520-2

Mari, M., Griffith, J., Rieter, E., Krishnappa, L., Klionsky, D. J. and Reggiori, F. (2010). An Atg9-containing compartment that functions in the early steps of autophagosome biogenesis. *J. Cell Biol.* **190**, 1005-1022. doi:10.1083/jcb.200912089

Mastronarde, D. N. (1997). Dual-axis tomography: an approach with alignment methods that preserve resolution. *J. Struct. Biol.* **120**, 343-352. doi:10.1006/jsbi.1997.3919

Mastronarde, D. N. (2003). SerialEM: a program for automated tilt series acquisition on tecnai microscopes using prediction of specimen position. *Microsc. Microanal.* **9**, 1182-1183. doi:10.1017/S1431927603445911

Matoba, K., Kotani, T., Tsutsumi, A., Tsuji, T., Mori, T., Noshiro, D., Sugita, Y., Nomura, N., Iwata, S., Ohsumi, Y. et al. (2020). Atg9 is a lipid scramblase that mediates autophagosomal membrane expansion. *Nat. Struct. Mol. Biol.* **27**, 1209. doi:10.1038/s41594-020-00518-w

Morin, A., Eisenbraun, B., Key, J., Sanschagrin, P. C., Timony, M. A., Ottaviano, M. and Sliz, P. (2013). Collaboration gets the most out of software. *eLife* **2**, e01456. doi:10.7554/eLife.01456

Morita, K., Hama, Y., Izume, T., Tamura, N., Ueno, T., Yamashita, Y., Sakamaki, Y., Mimura, K., Morishita, H., Shihoya, W. et al. (2018). Genome-wide CRISPR screen identifies *TMEM41B* as a gene required for autophagosome formation. *J. Cell Biol.* **217**, 3817-3828. doi:10.1083/jcb.201804132

Nakatogawa, H. (2020). Mechanisms governing autophagosome biogenesis. *Nat. Rev. Mol. Cell Biol.* **21**, 439-458. doi:10.1038/s41580-020-0241-0

Noda, N. N. (2024). Structural view on autophagosome formation. *FEBS Lett.* **598**, 84-106. doi:10.1002/1873-3468.14742

Noda, T., Kim, J., Huang, W.-P., Baba, M., Tokunaga, C., Ohsumi, Y. and Klionsky, D. J. (2000). Apg9p/Cvt7p is an integral membrane protein required for transport vesicle formation in the Cvt and autophagy pathways. *J. Cell Biol.* **148**, 465-480. doi:10.1083/jcb.148.3.465

Olivas, T. J., Wu, Y., Yu, S., Luan, L., Choi, P., Guinn, E. D., Nag, S., De Camilli, P. V., Gupta, K. and Melia, T. J. (2023). ATG9 vesicles comprise the seed membrane of mammalian autophagosomes. *J. Cell Biol.* **222**, e202208088. doi:10.1083/jcb.202208088

Orsi, A., Razi, M., Dooley, H. C., Robinson, D., Weston, A. E., Collinson, L. M. and Tooze, S. A. (2012). Dynamic and transient interactions of Atg9 with autophagosomes, but not membrane integration, are required for autophagy. *Mol. Biol. Cell* **23**, 1860-1873. doi:10.1091/mbc.e11-09-0746

Osawa, T., Kotani, T., Kawaoka, T., Hirata, E., Suzuki, K., Nakatogawa, H., Ohsumi, Y. and Noda, N. N. (2019). Atg2 mediates direct lipid transfer between membranes for autophagosome formation. *Nat. Struct. Mol. Biol.* **26**, 281-288. doi:10.1038/s41594-019-0203-4

Papinski, D., Schuschnig, M., Reiter, W., Wilhelm, L., Barnes, C. A., Maiolica, A., Hansmann, I., Pfaffenwimmer, T., Kijanska, M., Stoffel, I. et al. (2014). Early steps in autophagy depend on direct phosphorylation of Atg9 by the Atg1 kinase. *Mol. Cell* **53**, 471-483. doi:10.1016/j.molcel.2013.12.011

Rao, Y., Perna, M. G., Hofmann, B., Beier, V. and Wollert, T. (2016). The Atg1–kinase complex tethers Atg9-vesicles to initiate autophagy. *Nat. Commun.* **7**, 10338. doi:10.1038/ncomms10338

Ravikumar, B., Moreau, K., Jahreiss, L., Puri, C. and Rubinsztein, D. C. (2010). Plasma membrane contributes to the formation of pre-autophagosomal structures. *Nat. Cell Biol.* **12**, 747-757. doi:10.1038/ncb2078

Raymond, C. K., Howald-Stevenson, I., Vater, C. A. and Stevens, T. H., Ogris, E., Kraft, C. and Martens, S. (1992). Morphological classification of the yeast vacuolar protein sorting mutants: evidence for a prevacuolar compartment in class E vps mutants. *Mol. Biol. Cell* **3**, 1389-1402. doi:10.1091/mbc.3.12.1389

Romanov, J., Walczak, M., Ibiricu, I., Schüchner, S., Ogris, E., Kraft, C. and Martens, S. (2012). Mechanism and functions of membrane binding by the Atg5-Atg12/Atg16 complex during autophagosome formation: role of Atg5-Atg12/Atg16 during autophagy. *EMBO J.* **31**, 4304-4317. doi:10.1038/emboj.2012.278

Russell, M. R. G., Shideler, T., Nickerson, D. P., West, M. and Odorizzi, G. (2012). Class E compartments form in response to ESCRT dysfunction in yeast due to hyperactivity of the Vps21 Rab GTPase. *J. Cell Sci.* **125**, 5208-5220. doi:10.1242/jcs.111310

Sawa-Makarska, J., Baumann, V., Coudevylle, N., von Bülow, S., Nogellova, V., Abert, C., Schuschnig, M., Graef, M., Hummer, G. and Martens, S. (2020). Reconstitution of autophagosome nucleation defines Atg9 vesicles as seeds for membrane formation. *Science* **369**, eaaz7714. doi:10.1126/science.aaz7714

Schaffer, M., Mahamid, J., Engel, B. D., Laugks, T., Baumeister, W. and Plitzko, J. M. (2017). Optimized cryo-focused ion beam sample preparation aimed at in situ structural studies of membrane proteins. *J. Struct. Biol.* **197**, 73-82. doi:10.1016/j.jsb.2016.07.010

Schimmöller, F. and Riezman, H. (1993). Involvement of Ypt7p, a small GTPase, in traffic from late endosome to the vacuole in yeast. *J. Cell Sci.* **106**, 823-830. doi:10.1242/jcs.106.3.823

Schönnenbeck, P., Junglas, B. and Sachse, C. (2025). CryoVIA: an image analysis toolkit for the quantification of membrane structures from cryo-EM micrographs. *Structure* **33**, 808-819.e4. doi:10.1016/j.str.2025.01.013

Schütter, M., Giavalisco, P., Brodesser, S. and Graef, M. (2020). Local fatty acid channeling into phospholipid synthesis drives phagophore expansion during autophagy. *Cell* **180**, 135-149.e14. doi:10.1016/j.cell.2019.12.005

Shatz, O., Fraiberg, M., Isola, D., Das, S., Gogoi, O., Polyansky, A., Shimoni, E., Dadosh, T., Dezorella, N., Wolf, S. G. et al. (2024). Rim aperture of yeast autophagic membranes balances cargo inclusion with vesicle maturation. *Dev. Cell* **59**, 911-923.e4. doi:10.1016/j.devcel.2024.02.002

Shibutani, S. T. and Yoshimori, T. (2014). A current perspective of autophagosome biogenesis. *Cell Res.* **24**, 58-68. doi:10.1038/cr.2013.159

Shima, T., Kirisako, H. and Nakatogawa, H. (2019). COPII vesicles contribute to autophagosomal membranes. *J. Cell Biol.* **218**, 1503-1510. doi:10.1083/jcb.201809032

Shpilka, T., Welter, E., Borovsky, N., Amar, N., Mari, M., Reggiori, F. and Elazar, Z. (2015). Lipid droplets and their component triglycerides and steryl esters regulate autophagosome biogenesis. *EMBO J.* **34**, 2117-2131. doi:10.15252/embj.201490315

Stefan, C. J. and Blumer, K. J. (1999). A Syntaxin Homolog Encoded by VAM3 Mediates Down-regulation of a Yeast G Protein-coupled Receptor. *J. Biol. Chem.* **274**, 1835-1841. doi:10.1074/jbc.274.3.1835

Suzuki, K. and Ohsumi, Y. (2010). Current knowledge of the pre–autophagosomal structure (PAS). *FEBS Lett.* **584**, 1280-1286. doi:10.1016/j.febslet.2010.02.001

Suzuki, K., Akioka, M., Kondo-Kakuta, C., Yamamoto, H. and Ohsumi, Y. (2013). Fine mapping of autophagy-related proteins during autophagosome formation in *Saccharomyces cerevisiae*. *J. Cell Sci.* **126**, 2534-2544. doi:10.1242/jcs.122960

Takahashi, Y., He, H., Tang, Z., Hattori, T., Liu, Y., Young, M. M., Serfass, J. M., Chen, L., Gebru, M., Chen, C. et al. (2018). An autophagy assay reveals the ESCRT-III component CHMP2A as a regulator of phagophore closure. *Nat. Commun.* **9**, 2855. doi:10.1038/s41467-018-05254-w

Takeshige, K., Baba, M., Tsuboi, S., Noda, T. and Ohsumi, Y. (1992). Autophagy in yeast demonstrated with proteinase-deficient mutants and conditions for its induction. *J. Cell Biol.* **119**, 301-311. doi:10.1083/jcb.119.2.301

Tegunov, D. and Cramer, P. (2019). Real-time cryo-electron microscopy data preprocessing with Warp. *Nat. Methods* **16**, 1146-1152. doi:10.1038/s41592-019-0580-y

Thörnig, P. (2021). JURECA: data centric and booster modules implementing the modular supercomputing architecture at Jülich supercomputing centre. *J. Large-Scale Res. Facil.* **7**, A182. doi:10.17815/jlsrf-7-182

Toulmay, A., Whittle, F. B., Yang, J., Bai, X., Diarra, J., Banerjee, S., Levine, T. P., Golden, A. and Prinz, W. A. (2022). Vps13-like proteins provide phosphatidylethanolamine for GPI anchor synthesis in the ER. *J. Cell Biol.* **221**, e202111095. doi:10.1083/jcb.202111095

Tsukada, M. and Ohsumi, Y. (1993). Isolation and characterization of autophagy–defective mutants of Saccharomyces cerevisiae. *FEBS Lett.* **333**, 169-174. doi:10.1016/0014-5793(93)80398-E

Valverde, D. P., Yu, S., Boggavarapu, V., Kumar, N., Lees, J. A., Walz, T., Reinisch, K. M. and Melia, T. J. (2019). ATG2 transports lipids to promote autophagosome biogenesis. *J. Cell Biol.* **218**, 1787-1798. doi:10.1083/jcb.201811139

Van Vliet, A. R., Chiduza, G. N., Maslen, S. L., Pye, V. E., Joshi, D., De Tito, S., Jefferies, H. B. J., Christodoulou, E., Roustan, C., Punch, E. et al. (2022). ATG9A and ATG2A form a heteromeric complex essential for autophagosome formation. *Mol. Cell* **82**, 4324-4339.e8. doi:10.1016/j.molcel.2022.10.017

Van Vliet, A. R., Jefferies, H. B. J., Faull, P. A., Chadwick, J., Ibrahim, F., Skehel, M. J. and Tooze, S. A. (2024). Exploring the ATG9A interactome uncovers interaction with VPS13A. *J. Cell Sci.* **137**, jcs261081. doi:10.1242/jcs.261081

Wang, Y., Dahmane, S., Ti, R., Mai, X., Zhu, L., Carlson, L.-A. and Stjepanovic, G. (2025). Structural basis for lipid transfer by the ATG2A–ATG9A complex. *Nat. Struct. Mol. Biol.* **32**, 35-47. doi:10.1038/s41594-024-01376-6

Wen, X. and Klionsky, D. J. (2016). An overview of macroautophagy in yeast. *J. Mol. Biol.* **428**, 1681-1699. doi:10.1016/j.jmb.2016.02.021

Xie, Z. and Klionsky, D. J. (2007). Autophagosome formation: core machinery and adaptations. *Nat. Cell Biol.* **9**, 1102-1109. doi:10.1038/ncb1007-1102

Yamamoto, H., Kakuta, S., Watanabe, T. M., Kitamura, A., Sekito, T., Kondo-Kakuta, C., Ichikawa, R., Kinjo, M. and Ohsumi, Y. (2012). Atg9 vesicles are an important membrane source during early steps of autophagosome formation. *J. Cell Biol.* **198**, 219-233. doi:10.1083/jcb.201202061

Ylä-Anttila, P., Vihinen, H., Jokitalo, E. and Eskelinen, E.-L. (2009). 3D tomography reveals connections between the phagophore and endoplasmic reticulum. *Autophagy* **5**, 1180-1185. doi:10.4161/auto.5.8.10274

Young, A. R. J., Chan, E. Y. W., Hu, X. W., Köchl, R., Crawshaw, S. G., High, S., Hailey, D. W., Lippincott-Schwartz, J. and Tooze, S. A. (2006). Starvation and ULK1-dependent cycling of mammalian Atg9 between the TGN and endosomes. *J. Cell Sci.* **119**, 3888-3900. doi:10.1242/jcs.03172

Zanetti, G., Prinz, S., Daum, S., Meister, A., Schekman, R., Bacia, K. and Briggs, J. A. (2013). The structure of the COPII transport-vesicle coat assembled on membranes. *eLife* **2**, e00951. doi:10.7554/eLife.00951

Zheng, S., Wolff, G., Greenan, G., Chen, Z., Faas, F. G. A., Bárcena, M., Koster, A. J., Cheng, Y. and Agard, D. A. (2022). AreTomo: an integrated software package for automated marker-free, motion-corrected cryo-electron tomographic alignment and reconstruction. *J. Struct. Biol. X* **6**, 100068. doi:10.1016/j.yjsbx.2022.100068

Zhou, F., Wu, Z., Zhao, M., Murtazina, R., Cai, J., Zhang, A., Li, R., Sun, D., Li, W., Zhao, L. et al. (2019). Rab5-dependent autophagosome closure by ESCRT. *J. Cell Biol.* **218**, 1908-1927. doi:10.1083/jcb.201811173